

# JGR Solid Earth

## RESEARCH ARTICLE

10.1029/2022JB026260

### Key Points:

- We present the first continent-scale analysis of slowness vector deviations, slowness vector divergence, and multipathing
- We resolve seismically slow and fast structures such as slabs and hotspots and find tomography model NA13 fits our data best
- Slowness vector measurements are vital to study the Earth's mantle and we argue should be included in tomography inversions

### Supporting Information:

Supporting Information may be found in the online version of this article.

### Correspondence to:

J. Ward,  
J.Ward2@leeds.ac.uk

### Citation:

Ward, J., Thorne, M., Nowacki, A., & Rost, S. (2023). Upper mantle structure beneath the contiguous US resolved with array observations of SKS multipathing and slowness vector perturbations. *Journal of Geophysical Research: Solid Earth*, 128, e2022JB026260. <https://doi.org/10.1029/2022JB026260>

Received 12 DEC 2022

Accepted 16 JUN 2023





### Author Contributions:

**Conceptualization:** J. Ward  
**Data curation:** M. Thorne  
**Formal analysis:** J. Ward  
**Funding acquisition:** A. Nowacki, S. Rost  
**Investigation:** J. Ward  
**Methodology:** J. Ward  
**Project Administration:** A. Nowacki, S. Rost  
**Software:** J. Ward  
**Supervision:** M. Thorne, A. Nowacki, S. Rost  
**Validation:** J. Ward  
**Visualization:** J. Ward  
**Writing – original draft:** J. Ward

© 2023. The Authors.

This is an open access article under the terms of the [Creative Commons Attribution License](#), which permits use, distribution and reproduction in any medium, provided the original work is properly cited.

## Upper Mantle Structure Beneath the Contiguous US Resolved With Array Observations of SKS Multipathing and Slowness Vector Perturbations

J. Ward<sup>1</sup> , M. Thorne<sup>2</sup> , A. Nowacki<sup>1</sup> , and S. Rost<sup>1</sup> 

<sup>1</sup>School of Earth and Environment, University of Leeds, Leeds, UK, <sup>2</sup>Department of Geology and Geophysics, University of Utah, Salt Lake City, UT, USA

**Abstract** Continent-scale observations of seismic phenomena have provided multi-scale constraints of the Earth's interior. Of those analyzed, array-based observations of slowness vector properties (backazimuth and horizontal slowness) and multipathing have yet to be made on a continental scale. Slowness vector measurements give inferences on mantle heterogeneity properties such as velocity perturbation and velocity gradient strength and quantify their effect on the wavefield. Multipathing is a consequence of waves interacting with strong velocity gradients resulting in two arrivals with different slowness vector properties and times. The mantle structure beneath the contiguous United States has been thoroughly analyzed by previous seismic studies and is data-rich, making it an excellent testing ground to both analyze mantle structure with our approach and compare with other imaging techniques. We apply an automated array-analysis technique to an SKS data set to create the first continent-scale data set of multipathing and slowness vector measurements. We analyze the divergence of the slowness vector deviation field to highlight seismically slow and fast regions. Our results resolve several slow mantle anomalies beneath Yellowstone, the Appalachian mountains and fast anomalies throughout the mantle. Many of the anomalies cause multipathing in frequency bands 0.15–0.30 and 0.20–0.40 Hz which suggests velocity transitions over at most 500 km exist. Comparing our observations to synthetics created from tomography models, we find model NA13 (Bedle et al., 2021, <https://doi.org/10.1029/2021GC009674>) fits our data best but differences still remain. We therefore suggest slowness vector measurements should be used as an additional constraint in tomographic inversions and will lead to better resolved models of the mantle.

**Plain Language Summary** Observations of many phenomena such as reflections and scattering of waves generated by earthquakes have been analyzed on a continental scale. These observations have led to great progress in our understanding of the Earth's structure and dynamics. What has yet to be analyzed on such a large scale are the deflections of seismic waves at the boundaries of structures such as mantle upwelling. Analyzing these deflections can give information on the boundary structure of mantle structures. In this study, we present the first continent-scale data set of measurements quantifying the extent waves have been perturbed from their path between the earthquake and recording station. From this new data set, we infer the extent of the deflection is dependent on the spatial scale we are sensitive to. When analyzing our data set spatially, we find evidence for several potential mantle upwellings and fragmented subducted crust beneath the US. Our observations support previous models of the upper mantle beneath the US but differences remain suggesting observations of direction and velocity could improve the creation of these models. Our observations show mantle structure can be well resolved with measurements of wavefield deflection and that these measurements will be crucial for furthering our understanding of Earth structure and dynamics.

## 1. Introduction

Seismic phenomena analyzed on a continental scale have improved our understanding of whole-Earth dynamics. Such studies have analyzed reflectors in the mid mantle (e.g., Bentham et al., 2017; Deuss, 2009; Deuss et al., 2006; Waszek et al., 2018), converted phases (Abt et al., 2010; Jenkins et al., 2017), and small-scale heterogeneity from scattering (Hedlin & Shearer, 2000; Ma & Thomas, 2020; Waszek et al., 2015), from waveform complexity (Thorne et al., 2020, 2021), and through seismic tomography (Bedle et al., 2021; Fichtner et al., 2018; Schmandt & Lin, 2014; Sigloch et al., 2008). Using slowness vector measurements (backazimuth and horizontal slowness) to quantify diffraction and observe multipathing caused by mantle heterogeneity boundaries has yet to

**Writing – review & editing:** J. Ward, M. Thorne, A. Nowacki, S. Rost

be performed on a continental scale. Diffraction and multipathing are sensitive to the velocity gradient strength and velocity perturbations of the heterogeneity. As seismic velocity changes with both temperature and composition, these observations can give insight into the thermal and compositional gradients at the boundaries of these anomalies, and be used to test geodynamical hypotheses. Multipathing occurs when a wavefield is incident on a sufficiently strong velocity gradient that, over a short distance (100s km), the wave travels at different speeds and will be diffracted. This results in multiple distinct arrivals each with different arrival times and, because of the diffraction, with different horizontal velocities and directions (horizontal slownesses and backazimuths). Multipathing has been observed in slowness space in surface waves (Maupin, 2011) and body waves (Ward et al., 2020) and its effect on waveform complexity has been extensively studied (Ni et al., 2002; Ni & Helmberger, 2003; Sun et al., 2009, 2019; C. Zhao et al., 2015).

As slowness vector measurements of diffraction and multipathing have not been analyzed on a continental scale, we present the first study analyzing these phenomena using data sampling the mantle beneath the contiguous United States (US). The contiguous US has been studied intensely using travel-time (Schmandt & Lin, 2014; Shen & Ritzwoller, 2016; Sigloch et al., 2008) and full-waveform tomography (Krischer et al., 2018; Rodgers et al., 2022; Yuan et al., 2014; Zhou et al., 2022) as well as higher resolution studies using scattering (Ritsema et al., 2020), structure beneath seismic arrays (Capon, 1974) and receiver functions (e.g., Abt et al., 2010; Kind et al., 2015; Schmandt et al., 2014). These studies have shown the upper mantle is complex with the possible presence of mantle plumes (Porritt et al., 2014; Schmandt & Humphreys, 2010; Tao et al., 2020; Tian et al., 2009) and lithosphere fragments (Biryol et al., 2016; Bunge & Grand, 2000; Grand et al., 1997; Pierce & Morgan, 2009; Sigloch et al., 2008; Tian et al., 2011; Wang et al., 2019). The contiguous US has an abundance of data, has been heavily studied and has complex mantle structure. Therefore, it is an excellent location to perform the first continental-scale analysis of mantle structure using slowness vector measurements and multipathing. We do this with minimal need for visual inspection by applying the automated array technique of Ward et al. (2021) to a continental-scale SKS data set taken from Thorne et al. (2020), densely sampling beneath the US.

We perform the analysis over three frequency bands each sensitive to different length scales and make 5,960 observations (Table S1 in Supporting Information S1). We first analyze the frequency dependence of multipathing observed by Ward et al. (2020) and slowness vector deviation magnitude, and then analyze the data set spatially. Forward modeling results show fast seismic anomalies cause slowness vector deviations to have a converging pattern and a slow seismic anomaly to have a diverging pattern (see Section 4.1). Therefore, we analyze slowness vector deviations by taking the divergence to highlight regions of fast or slow mantle heterogeneities. We observe slowness vector deviations indicative of fast and slow anomalies in the North American upper mantle possibly caused by subducted slab fragments, the Yellowstone anomaly and the Northern Appalachian Anomaly. We find multipathing is present at the boundaries of many heterogeneities in the highest frequency band (0.20–0.40 Hz) and anomalies that have been interpreted as lying between the 410 and 660 transition zone depths show multipathing strongly in the 0.15–0.30 Hz frequency band. Future work can focus on exploring the relationship between frequency dependence of multipathing and stagnating slabs as well as the incorporation of slowness vector measurements into tomographic inversions.

## 2. Methods

### 2.1. Data and Sub-Arrays

We used a subset of the global SKS data set of Thorne et al. (2020), which included events between 1990 and 2017 with magnitudes greater than 5.8, deeper than 75 km and with epicentral distances between 90° and 130°. SKS has several advantages to study mantle structure. As shown in our modeling later, source-side mantle structure has little effect on the slowness vector measurement. The outer core is assumed to be well mixed and have a radial seismic structure so it should not affect slowness vector measurements. SKS has a near vertical incidence, therefore when interpreting the results, one can assume a wave exits the core and travels steeply through the mantle, making SKS sensitive to lateral velocity gradients. A disadvantage of using SKS is it is challenging to infer the depth or depth extent of the heterogeneities we find. In the future, using other phases with other incidence angles in combination with SKS may constrain heterogeneity depths better.

The raw data were processed as described in Thorne et al. (2020) by removing the mean and trend then the instrument response. Low-quality data were removed first with an ensemble of neural networks each trained on

the amplitude spectra of 10,000 traces and their respective labels of high or low quality following the approach of Valentine and Woodhouse (2010). Following this, all traces were visually inspected for quality and the high-quality traces were kept for analysis. For each event, the stations recording high-quality data were divided into sub-arrays using the following approach.

To ensure high-quality observations, we required a sub-array to have a minimum of 15 stations with a maximum aperture of 400 km. To ensure all sub-arrays met these criteria, we first used density-based clustering algorithm DBSCAN (Ester et al., 1996) to remove stations which do not meet the criteria defined above. DBSCAN (Ester et al., 1996) is a density-based clustering algorithm that classified the station locations into “core” stations, which have at least 15 other stations within 200 km of it, “boundary” stations which did not meet the density criteria but are within the 200 km neighborhood of a core station and “outlier” stations which did not meet the density criteria and were not in the 200 km neighborhood of a core station. The outlier stations were removed and not used to make sub-arrays. We spatially resampled the core stations such that none were within 200 km of each other. This was done by randomly selecting a core station, recording it as a centroid station, removing all core stations within 200 km of it and randomly moving to another core station. This continued until all stations are centroid stations or removed as candidates to be centroid stations. For each of the centroid stations, we created a sub-array made up of all stations within 200 km of it. Figure S1 in Supporting Information S1 illustrates the steps to form sub-arrays and Figure 1 shows the resulting sub-array locations with the events and sampling of SKS in the lower mantle.

## 2.2. Automatic Multipathing and Slowness Vector Measurements

For each event–sub-array combination, we used the method of Ward et al. (2021) to automatically identify multipathed and single arrivals in slowness space and measure their slowness vector properties. Here, we provide a brief summary of the method but for details, such as searching for optimal parameters, see Ward et al. (2021).

The waveforms recorded at a seismic array from which the measurement is to be made are bootstrap sampled (Efron, 1992) into  $N$  (1,000 here) sub-samples. For each of the  $N$  bootstrap samples, we use beamforming (Rost & Thomas, 2002) corrected for a curved wavefront (Ward et al., 2020) to calculate the coherent power at a range of slowness vector properties. From this power distribution in slowness-space, take the top  $M$  power maxima (3 here) above a noise estimate. The location of the maxima in slowness space gives their slowness vector properties. For the sake of ease of explanation, we describe slowness vector properties as points in a 2-D slowness-space. Each bootstrap sample will have its own power distribution and respective points. Gather all points from each of the bootstrap samples and use DBSCAN (Ester et al., 1996), to identify arrivals as dense clusters of the points. DBSCAN parameters  $\epsilon$  and  $MinPts$  define the density threshold to identify the clusters where at least  $MinPts$  points need to be within a radius  $\epsilon$  for a region to be defined as a cluster. We set the DBSCAN parameters  $\epsilon$  and  $MinPts$  as 0.20 s/° and 250 points respectively in line with the tuning from Ward et al. (2021). The number of clusters found is taken as the number of arrivals, the mean of the location of the points in each cluster gives the slowness vector properties of the arrival and the scatter of the points in each cluster gives the uncertainty estimates of the slowness vector measurement. Figure S2 in Supporting Information S1 illustrates the method.

By using this method, we can confidently make slowness vector measurements of a large data set and identify multipathing. We define multipathing as more than one SKS arrival being found within the 40 s time window by the method outlined above and be within 3 s/° of the PREM predicted slowness vector properties. Observations classified as multipathed were visually inspected to check the classification and if necessary relabeled. Multipathing from lower mantle structure has been observed to be frequency-dependent (Ward et al., 2020) suggesting the Fresnel zone size relative to the velocity gradient sharpness of the boundary may impact whether multipathing is observable or not. Therefore, constraining in which frequency band multipathing is observable may give an indication of the velocity gradient sharpness or depths due to the variation of the Fresnel zone with depth as well as frequency. To identify velocity gradients of different sharpness and strength, we conduct this analysis in three frequency bands (0.10–0.20 Hz, 0.15–0.30 Hz, 0.20–0.40 Hz). In total there were 5,960 observations. The breakdown of the number of multipathed and single arrivals in each frequency band is shown in Table S1 in Supporting Information S1.

Instead of analyzing backazimuth and horizontal slowness deviations, we analyzed slowness vector deviations. We define the slowness vector deviation as the vector from the predicted location in slowness space to the observed location as shown in Figure 2. The larger the magnitude of the vector, the further the observation is from the PREM (Dziewonski & Anderson, 1981) prediction.

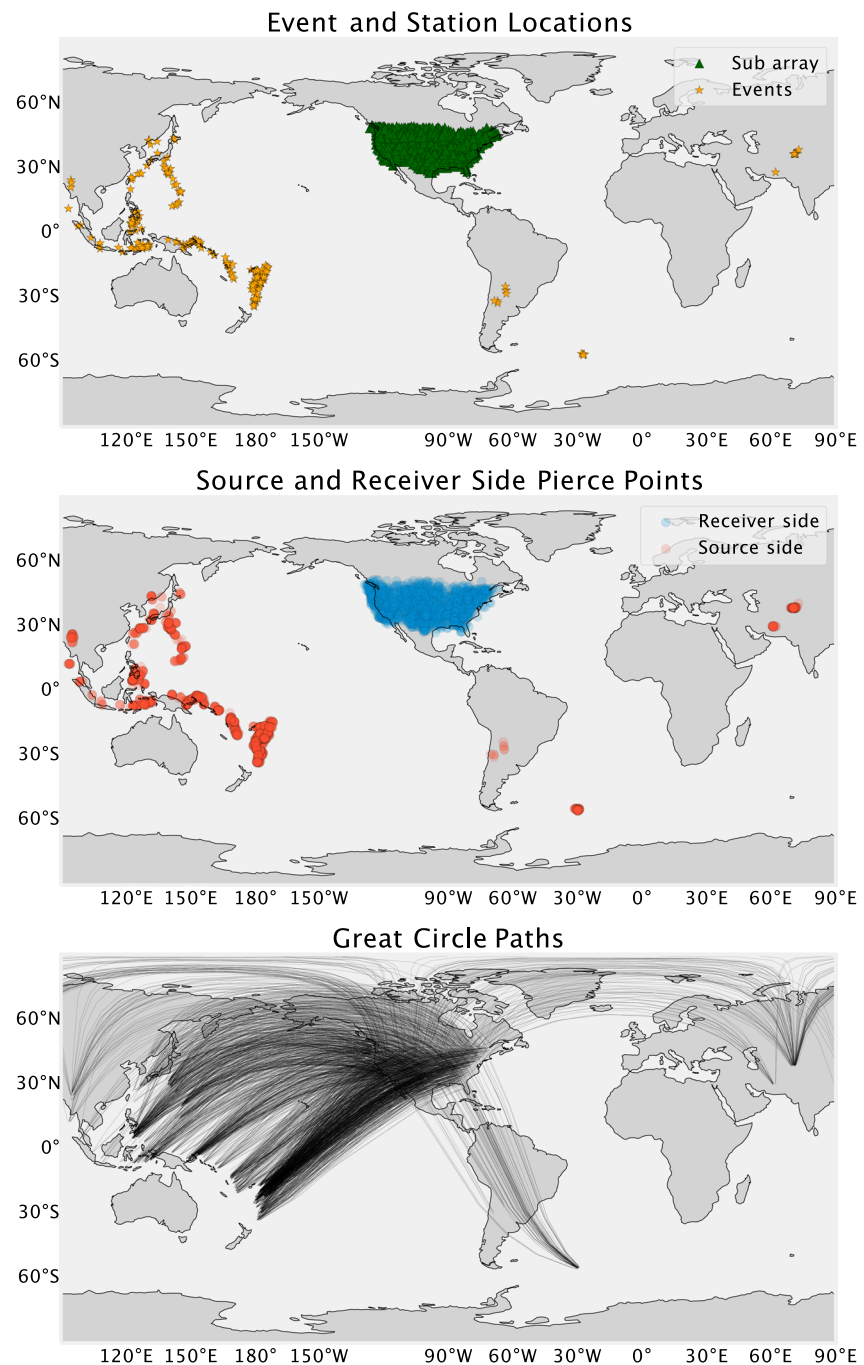


**Figure 1.** Top: Event (orange stars) and sub-array (green triangles) coverage of the high-quality observations after applying the method from Ward et al. (2021). Middle: map of SKS pierce point coverage at 2800 km depth for the observations after applying the method of Ward et al. (2021). Blue and red circles show the pierce point location on the receiver- and source-side, respectively. Bottom: great circle paths from event to stations.

### 2.3. Constraining Velocity Gradient Depth

A challenge with interpreting SKS slowness vector measurements and multipathing locations is determining the depth of the structure causing the wavefield perturbations and whether it is on the source- or receiver-side. Furthermore, interpretation becomes more complex as there could be multiple structures affecting the wavefield at different depths and locations. The unique sampling density we are able to achieve in this data set allows us

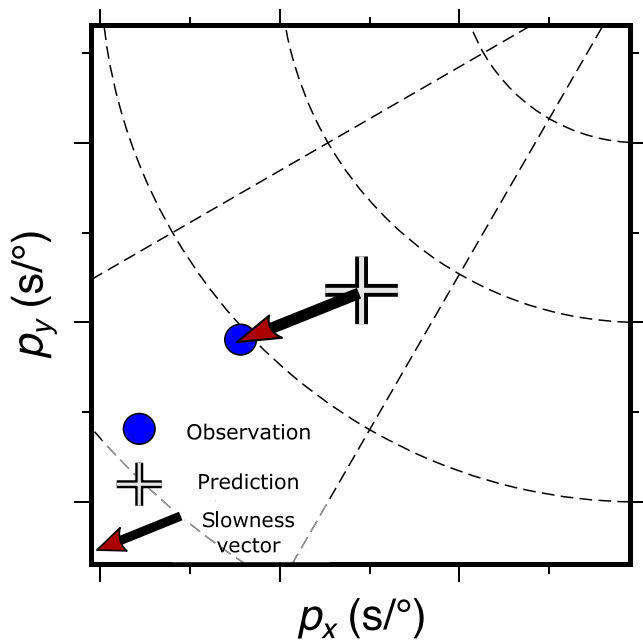


**Figure 2.** Cartoon illustrating our definition of the slowness vector deviation.  $p_x$  is the horizontal slowness in the east-west direction and  $p_y$  is the horizontal slowness in the north-south direction. The slowness vector deviation is the vector from the PREM (Dziewonski & Anderson, 1981) predicted arrival location in slowness space (black and gray cross) to the location of the observed arrival (blue circle).

for the first time to attempt to constrain the depth and location (source or receiver) of heterogeneities with the following approach.

For this analysis, assuming there is a single dominant structure causing the perturbation, we assume waves that sample similar regions should arrive with a similar slowness vector deviation as defined in Figure 2. The backazimuth and horizontal slowness deviations will vary with sampling azimuth but the vector which describes the full slowness vector deviation, as shown in Figure 2, will not. This is because the slowness vector deviation is orthogonal to the velocity gradient that causes the wave to diffract regardless of the sampling azimuth as we show later through forward modeling in Section 4.1. We quantified the similarity of slowness vector deviations of all observations sampling within 200 km bins by calculating their variance. The variance ( $\sigma^2$ ) of the slowness vector measurements is calculated as the mean square distance between all the slowness vectors and the mean as

$$\sigma^2 = \frac{\sum_i^N \left( \sqrt{(\bar{p}_x - p_{ix})^2 + (\bar{p}_y - p_{iy})^2} \right)^2}{N}, \quad (1)$$

where  $N$  is the number of vectors in the bin,  $\bar{p}_x$  and  $\bar{p}_y$  are respectively the east and north components of the mean slowness vector in the bin, and  $p_{ix}$  and  $p_{iy}$  are respectively the east and north components of the  $i$ th slowness vector measurement in the bin. The distances between the mean slowness vector and each of the slowness vector measurements are illustrated in Figure S3 in Supporting Information S1. When calculating the variance, we relocated the pierce point from its great circle path to the location it would travel from such that it arrived with the observed backazimuth and horizontal slowness (Ward et al., 2020).

We identified depths where mantle heterogeneities may be present by calculating the number of bins with a statistically significantly low variance. We did this by projecting the slowness vector measurements along their theoretical raypath from PREM to the depth in question, taking all observations within 100 km of the bin centre, and calculating the variance of the measurements in each bin as described in Equation 1. To infer which variances are statistically significantly low, we randomly took 20 slowness vector measurements from the whole data set and calculated the variance. This was repeated 1,000 times and the 5th percentile of these 1,000 random variance estimates is recorded. Variances lower than the 5th percentile estimate are labeled as significantly low and counted for that depth.

We infer which depths are likely to have heterogeneity from histograms of the number of low-variance bins with depth (Figure 5). From the histogram, we took the depths with more low-variance bins than the adjacent depths and analyzed the slowness vector deviations spatially. This approach gives an approximation about which depths may have mantle heterogeneity and attempts to address the poor depth resolution of SKS. Observations from other phases such as direct S wave arrival should be incorporated in the future to further improve the depth resolution.

The variance analysis could be repeated by analyzing the relative slowness vectors of the multipathed arrivals in the same observations. Different slowness vector properties would manifest itself as different locations in slowness space and these relative locations of the multipathed arrivals is indicative of the velocity gradient orientation that caused them (Ward et al., 2020). The slowness-space locations of the multipathed arrivals can be quantified by the azimuth between the locations in slowness space. If the same velocity gradient causes the multipathing in several observations, we expect the multipathed arrivals to have similar relative locations in slowness space. We could perform similar variance analysis to that performed earlier on the azimuths between the multipathed arrivals that sample a similar region. We did not do this as most regions show few multipathed arrivals to reliably calculate the variance.

#### 2.4. Estimating Velocity Gradient Length Scales

Once multipathing is observed, we cannot infer properties of the velocity gradient which caused it without computationally expensive finite-frequency forward modeling. We can, however, give an upper bound of the



length scale of the transition from the ambient mantle to the interior of the heterogeneity. When we present our multipathing observations and discuss possible causes we will give an estimate of the upper bound of the lateral velocity gradient extent. We do this by calculating the total area the array of stations is sensitive to in the mantle at the depth from which we hypothesize the multipathing comes.

We calculate the Fresnel zone diameter using

$$d = 2\sqrt{\frac{z\lambda}{2}}, \quad (2)$$

where  $d$  is the Fresnel zone diameter at depth  $z$ . The wavelength  $\lambda$  is calculated from the lower end of the frequency band in which multipathing has been observed (0.10, 0.15, or 0.20 Hz) and the PREM (Dziewonski & Anderson, 1981) velocity value at depth  $z$ . To find the upper bound of the velocity gradient length scale, this needs to be added to the diameter of the sub-array used for the recording, which we set as 400 km (Section 2.1). The diameter to which the array measurement is sensitive will change with depth. For example, a region spanning 400 km at the surface will become approximately 370 km when projected to the 410 transition zone. Therefore, this is accounted for before adding to the diameter of the Fresnel zone. With this, we propose maximum length scales for the lateral velocity gradients of heterogeneity observed.

## 2.5. Calculating the Divergence of the Slowness Vector Field

Results of forward modeling (Section 4.1) show the divergence of slowness vector deviations is indicative of whether the velocity anomaly is positive or negative. Therefore, we calculated the divergence over the grid of binned slowness vectors using

$$\nabla \cdot p = \frac{\delta p_x}{\delta x} + \frac{\delta p_y}{\delta y}, \quad (3)$$

where  $\delta p_x$  represents the differential of the east-west slowness vector component ( $p_x$ ) of longitudinally adjacent slowness vector bins,  $\delta x$  is the spacing of the slowness vectors with longitude,  $\delta p_y$  is the differential of the north-south slowness vector component ( $p_y$ ) of laterally adjacent slowness vector bins and  $\delta y$  is the latitude spacing. A positive divergence is expected for a low-velocity anomaly and a negative divergence for a high-velocity anomaly (see Section 4.1).

The grid spacing in longitude and latitude is 200 km and we calculated the divergence between the adjacent slowness vector components only. We assume the spacing between vectors is small enough that the effect of a spherical surface can be ignored. The divergence is plotted in the background of the slowness vector maps and can be used to infer the location of fast or slow anomalies. We can not directly relate the magnitude of divergence to the magnitude of the velocity anomaly, but this could be the basis of future work.

## 2.6. Limitations

This work is partly limited by the decisions made to automate the sub-array creation step and in the cluster analysis parameters used in the method of Ward et al. (2021). The maximum size of the sub-arrays, the minimum number of stations needed for a sub-array and the spacing of the sub-arrays will affect the number and distribution of the sub-arrays. The parameters were chosen such that each sub-array has sufficient stations to provide reliable observations while maximizing the coverage of the mantle without such heavy sampling that some observations are nearly redundant.

The parameters given to the automated method of Ward et al. (2021) to make the slowness vector measurements and identify multipathing is another limitation. Choosing the parameters requires a balance between finding as many low amplitude arrivals as possible while minimizing the misclassification of noise as arrivals. The parameters used in this study were taken from the tuning in Ward et al. (2021) which were shown to agree the most with a human-labeled data set and are best suited to this automated task.

Another limitation is the size of the bins chosen for the variance analysis and plotting. For the variance analysis, the size of the bin should be on the spatial scale expected for coherent slowness vector values to exist. A bin

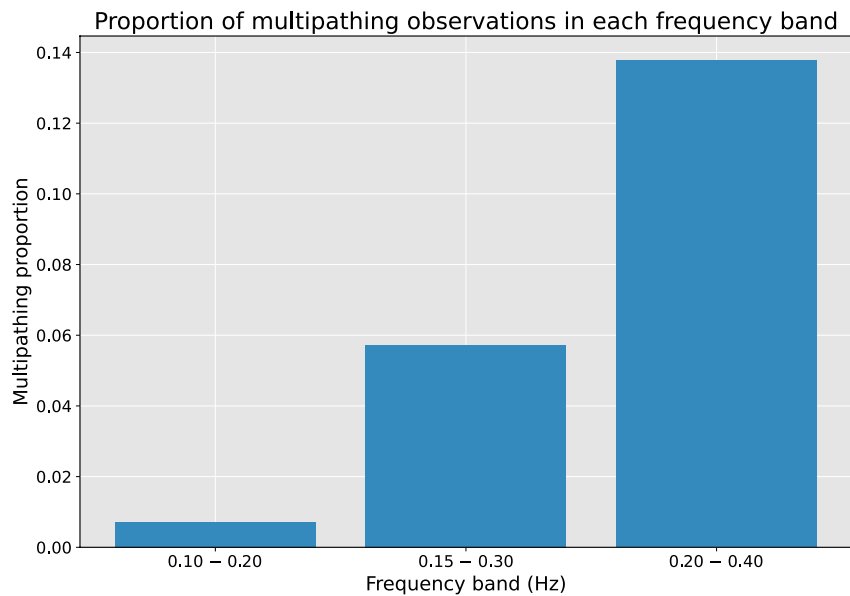


**Figure 3.** Histogram of the proportion of multipathing observations present in each frequency band. There is a clear trend of more multipathed arrivals observed at higher frequencies.

size that is too large may include many slowness vector values and may result in high variance and the removal of those observations. For plotting, too large a bin size or spacing would lose spatial resolution. For both the plotting and variance analysis, too small a bin size would mean there may be too few measurements to form a bin to make reliable variance estimates (here we require at least 10 values in a bin to use it) limiting the spatial coverage. To choose the bin size, the smallest bin size was chosen which retained enough coverage over the contiguous US while still having at least 10 observations per bin.

We used a constant time window of 20 s before and after the PREM (Dziewonski & Anderson, 1981) predicted arrival time which may have led to missing some SKS arrivals if they arrived very abnormally early or late and may have missed some multipathed arrivals. The time window was chosen to avoid contamination by other arrivals, such as SKKS. Due to the dense coverage of the data, we do not expect missing some arrivals in extreme cases will greatly affect our results.

### 3. Results—Frequency Dependence of Multipathing and Slowness Vector Perturbation

After processing, we have 5,960 observations over three frequency bands of backazimuth deviations, horizontal slowness deviations, multipathing presence and slowness vector deviation (Table S1 in Supporting Information S1). The average standard deviations of these measurements are 1.62° and 0.13 s/° showing the effects of array aperture, station spacing, and near-surface heterogeneity have little effect on these observations. In this section, we present these measurements and describe any patterns present.

#### 3.1. Frequency Dependence of Multipathing

Frequency dependence of multipathing has been observed previously with array methods by Ward et al. (2020) and was interpreted as a result of different velocity contrasts, spatial scales or depths. In our observations, we observe clear frequency dependence of multipathing (Figure 3) with the most multipathing observed in the highest frequency band and the least multipathing observed in the lowest frequency band. From this, we infer that velocity gradients on a relatively short spatial scale are more common in the US mantle. The precise length scale of the velocity gradient will be depth-dependent. We can give a maximum spatial scale for these velocity gradients at a given depth by calculating their Fresnel zone diameter over the whole sub-array (see Section 2.4). For velocity gradients in the upper mantle, where we hypothesize most multipathing is taking place due to the high number of low variance bins in the upper mantle, we suggest the maximum scale for the velocity gradient

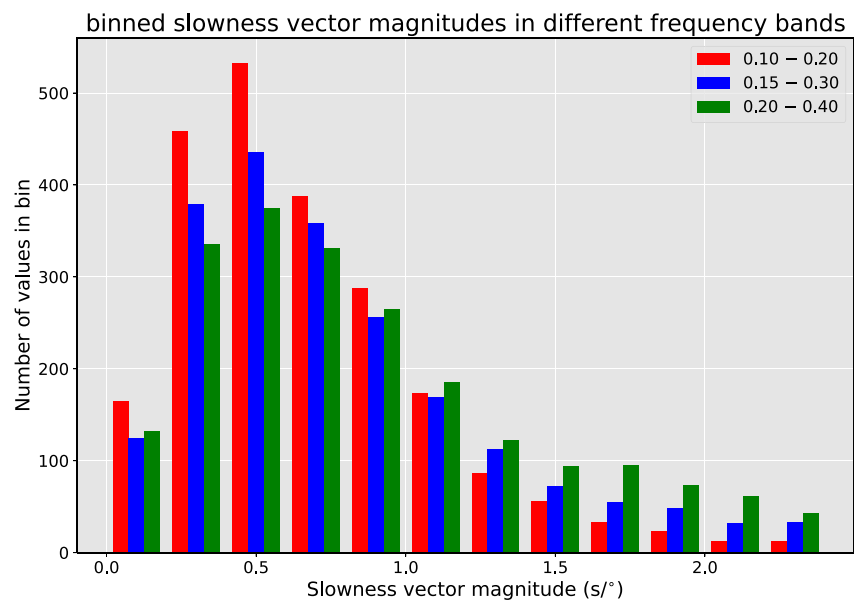


**Figure 4.** Histogram of slowness vector magnitudes binned in  $0.2 \text{ s}^\circ$  bins and colored by frequency band. There is a clear frequency dependence of slowness vector deviation magnitudes. Lower frequency bands (red) appear to have smaller slowness vector deviations and higher frequency bands (green) appear to have larger slowness vector deviations.

could be approximately 500, 480 and 470 km respectively for frequency bands 0.10–0.20 Hz, 0.15–0.30 Hz and 0.20–0.40 Hz.

### 3.2. Frequency Dependence of Slowness Vector Deviation Magnitude

We bin the magnitudes of the slowness vector deviations in  $0.1 \text{ s}^\circ$  bins to investigate whether there is any frequency dependence on slowness vector deviation magnitude (Figure 4). We observe evidence for a frequency dependence on slowness vector deviation magnitude with more low magnitude slowness vector deviations observed in the lowest frequency band and more large magnitude slowness vector deviations observed in the highest frequency band. This pattern could allow broad-scale properties of mantle velocity gradients to be constrained if it is replicated through forward modeling studies.

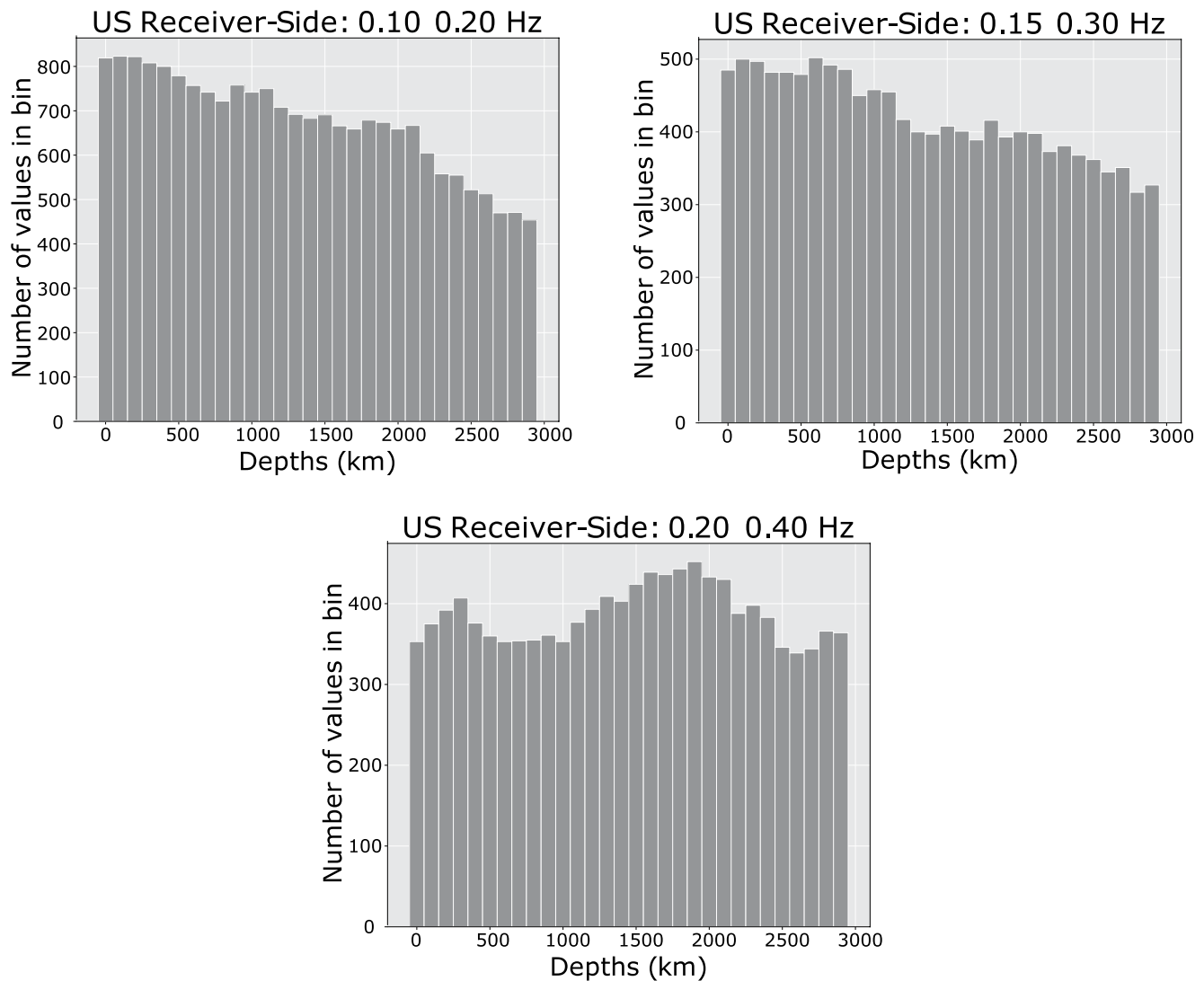
## 4. Results—Spatial Analysis and Forward Modeling

Figure 5 shows the results of the variance-depth analysis (Section 2.3) of the data set sampling the mantle beneath the US. There is little evidence for lower-mantle structure causing slowness vector deviations in our observations in the low and central frequency bands (0.10–0.20 and 0.15–0.30 Hz), because there are very few bins with low variance in the lower mantle suggesting no coherent pattern at this depth. However, the highest frequency band (0.20–0.40 Hz) contains several regions of high coherency, and as well as structure at  $\sim 300$  km depth, it appears to be sensitive to mid- and lower-mantle structure. We identify depths that may have mantle heterogeneity by those which have a higher number of low-variance bins than surrounding depths in the histograms (Figure 5). This is best shown in the 0.20–0.40 Hz band in Figure 5, where there are high bin counts at 400 km, 1,300–2,000 km and 2,800 km depth. The depth slices analyzed are listed in Table 1.

We perform the same variance analysis on the source-side paths of the data. While many bins have significantly low variance, most are low-magnitude slowness vectors ( $<0.5 \text{ s}^\circ$ ) and are not indicative of sampling mantle heterogeneity.

In the following sections, we first infer what the expected slowness vector deviation observation is for seismically slow and fast heterogeneity. Then, we present our observations at selected depth slices highlighting possible mantle heterogeneity. Following this, our observations are compared to synthetically generated data using three upper mantle tomography models (Bedle et al., 2021; Fichtner et al., 2018; Schmandt & Lin, 2014). This allows





**Figure 5.** Histograms of the number of bins with a significantly low variance of slowness vector measurements (Section 2.3) at each depth. These have been separated for each frequency band.

us to evaluate the tomography models, our data, and, as these are upper mantle models, the relative contribution of upper and lower mantle heterogeneity to the observations.

#### 4.1. Forward Modeling Tests

Before interpreting the observations spatially, we use 3-D ray-tracing (Simmons et al., 2011, 2012; D. Zhao et al., 1992) to infer the qualitative pattern of slowness vector deviations of seismically fast or slow mantle heterogeneity on the scale of 100s of kilometres.

For a qualitative comparison, ray tracing is sufficient as we do not seek to compare the modeling quantitatively with our observations. The outputs of the ray-tracing approach used here hold no information about the amplitudes of the arrivals, therefore it is unclear if the arrivals will arrive with enough power to be observed. A direct comparison of the modeling with the data would require finite frequency modeling which is beyond the scope of this work. Figure S4 in Supporting Information S1 shows an example model setup of the anomalies at the CMB with the event and station locations. The fast anomaly has a length of 1,000 km east to west, a length of 750 km north to

**Table 1**  
*Depths With Possible Mantle Heterogeneity Inferred From the Slowness Vector Variances*

Frequency band (Hz)	Depths analyzed
0.10–0.20	200, 1,000, 1,800, 2,000 km
0.15–0.30	200, 800, 1,000 km
0.20–0.40	300, 1,800, 2,891 km

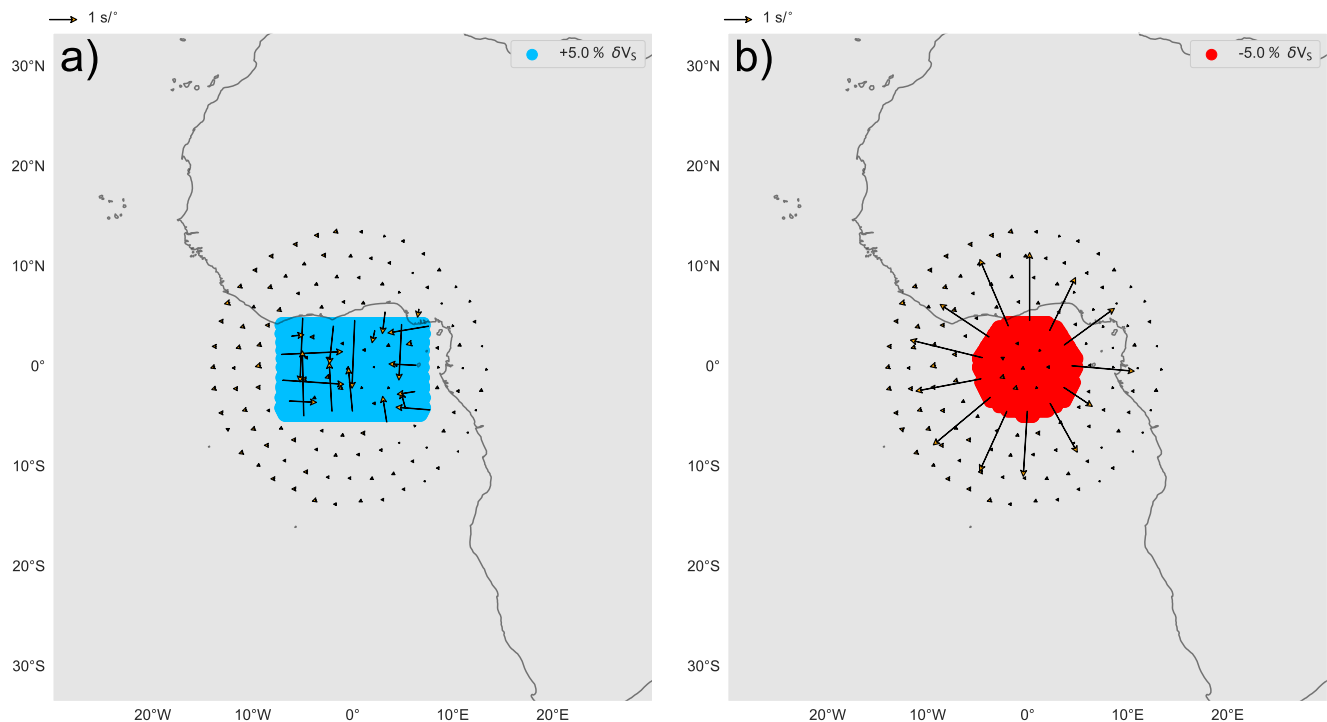


**Figure 6.** Slowness vector residuals for a fast cuboid (a) and a slow cylinder (b) with model setups shown in Figure S4 in Supporting Information S1. The fast cuboid has a depth extent of 300 km from 100 to 400 km depth, a length of 1,500 km and a width of 1,000 km and a velocity perturbation of  $+5 \delta V_s$ . The slow cylinder has a depth extent of 300 km between 100 and 400 km, a radius of 500 km and a velocity perturbation of  $+5 \delta V_s$ . Note, the slowness vector patterns for the slow cylinder show a diverging pattern and for the fast box a converging pattern. In all instances, the slowness vector azimuths are orthogonal to the boundary of the structure.

south and a height of 500 km above the CMB, with an S-wave velocity perturbation of  $+5\%$ . The slow anomaly is a cylinder with a diameter of 1,000 km, a height of 500 km above the CMB and an S-wave velocity perturbation of  $-5\%$  relative to PREM (Dziewonski & Anderson, 1981). The rest of the model takes the velocities of PREM. To test the effect of velocity anomaly perturbation we vary the anomaly strength to be  $+2.5$  and  $+10\%$  for the fast anomaly and  $-2.5$  and  $-10\%$  for the slow anomaly. We also test a smaller anomaly with a maximum diameter of 500 km and with an anomaly of  $+5$  and  $-5\%$  respectively. For each of these models, we investigate the effect they have when placed on the source and receiver side. We find receiver-side structure has a much greater effect on the slowness vector deviation. We discuss the effects of these further in the Supporting Information S1.

We calculate the arrival times at each station and insert a Ricker wavelet (Ricker, 1943, 1944) with a frequency of 0.15 Hz at the arrival times creating synthetic seismograms. Using the synthetic data, a beamforming grid search is conducted over a range of slowness vectors for each sub-array. We record the slowness vector properties with the highest power value and calculate the deviation from the PREM-predicted slowness vector properties. The differential slowness vector is plotted at the great circle path pierce points between the event and sub-array centre at the CMB. In addition to marking the slowness vector residuals at the great circle path pierce points, the vectors are relocated to the path through which they are inferred to travel in a 1-D Earth, such that they arrive with the slowness vector properties as the observation (as in Ward et al., 2020). This allows us to visualize possible origins of the wave after diffraction in the same way as the slowness vector plots in Section 4.2.

The slowness vector deviations for both model setups are shown in Figure 6. The modeling results clearly show a diverging pattern for the slow anomaly and a converging pattern for the fast anomaly. In both models, the slowness vector azimuths are perpendicular to the orientation of the boundary, are large at the edges of the structure and have a low magnitude in the centre of them. This suggests refraction through the centre of the heterogeneity is not enough to cause slowness vector deviations and that slowness vector measurements are only sensitive to the diffraction at the boundaries of the heterogeneities. Larger slowness vector deviation magnitudes are observed for a greater velocity perturbation and smaller deviation magnitudes for weaker velocity perturbations. For a smaller-sized anomaly, the results suggest the magnitude of the deviations is similar, but the area they are spread over is smaller supporting our interpretation that we are resolving the effects of boundary structure.

We test the effect of source-side structure in our synthetic testing where we use the same anomaly sizes and shapes but find negligible slowness vector deviation magnitudes except in the most extreme case with velocity anomalies of 10% with a height of 500 km and maximum width of 1,000 km. In this case, we find slowness vector deviations of at most  $0.5 \text{ s}^\circ$ . As this is the most extreme of the test anomaly cases, we do not think the source-side structure is contributing significantly to our observations. We discuss this further in Section S5 in Supporting Information S1.

## 4.2. Spatial Observations of Slowness Vectors and Multipathing

Using the results of Section 4.1, we present the slowness vector deviations and multipathing spatially. Multipathing and slowness vector deviation measurements provide different information about the heterogeneity. The presence or lack of multipathing in one or multiple frequency bands constrains the sharpness of the velocity gradient. The relative location of the multipathed arrivals in slowness space may give the orientation of the velocity gradient. It is challenging to recover the velocity anomaly of the heterogeneity through slowness space observations of multipathing alone. Slowness vector measurements on the other hand can give inferences on whether the heterogeneity is seismically fast or slow and the azimuth of the vectors can be used to infer the orientation of the boundary. Therefore, when analyzing velocity gradients in the mantle it is important to use both.

We only analyze slowness vector measurements that have a variance lower than the significant variance estimate and are then binned in 200 km-radius bins. The bin size was chosen to maximize clarity while retaining as much detail as possible. The multipathing observations are shown as the proportion of multipathing within 200 km bins with a minimum of 10 observations required to form a bin. Where multipathing is observed, we can estimate the maximum scale of the velocity gradient given the depth and frequency band it is observed in by taking the approach outlined in Section 2.4. To highlight the location of possible heterogeneity, the divergence of the slowness vector field is calculated with the approach discussed in Section 2.5.

### 4.2.1. Distribution of Slowness Vector Deviations and Multipathing Beneath the Contiguous US

In this section, we show the spatial distribution of multipathing and slowness vector deviations at selected depths and frequency bands with the remaining depths and frequency bands given in the supplementary material. Possible mantle heterogeneity is highlighted, with a geological interpretation presented later (Section 5). Figures 7 and 8 show the observations at 200 km depth and show several regions of strong divergence and high multipathing proportion.

We find the strongest positive divergence region (D1, Figure 7a) with large vector deviation magnitude ( $>1 \text{ s}^\circ$ ) and moderately high multipathing proportion (40%; M5 in Figure 8a) in the upper mantle beneath the Yellowstone region. Adjacent to the D1 anomaly, there are regions of high convergence (C1 and C2). The magnitudes of the slowness vectors around C1 vary depending on location with small magnitudes of  $<0.5 \text{ s}^\circ$  on the west and other regions showing large magnitudes of up to  $1.5 \text{ s}^\circ$ . The C2 anomaly shows more consistent slowness vector magnitudes of approximately  $1 \text{ s}^\circ$  at all azimuths and is also near a region of high multipathing proportion (50%) in the central frequency band (M8 in Figure 8b). The M8 anomaly has its highest proportion at depths shallower than 600 km and a much lower proportion deeper in the mantle (Figure 8c). At a depth of 500 km and in the frequency band of 0.15–0.30 Hz, we estimate the maximum transition length over which the velocity varies to be 530 km.

On either side of the C2 anomaly there are regions of strong positive divergence (D2 and D3) with slowness vector deviations of up to  $0.7 \text{ s}^\circ$ , suggesting seismically slow material where small-scale upwellings have been hypothesized by some (e.g., Schmandt et al., 2012). These regions show little multipathing, indicating either there are no sharp velocity gradients or they do not have the depth extent to cause multipathing in the slowness domain.

In the central and eastern US, we observe regions of converging slowness vector residuals with low magnitude residuals ( $\leq 0.2 \text{ s}^\circ$ ) surrounding them. These converging patterns (C4 and C5) suggest seismically fast material is present and similar anomalies in other studies have been interpreted as lithospheric fragments (Biryol et al., 2016; Sigloch et al., 2008; Wang et al., 2019). As these regions are not near any diverging patterns we do not think they are an artifact of nearby measurements. These regions have different multipathing characteristics depending on the frequency band. The C4 anomaly shows a high multipathing proportion (60%, M3 in Figure 8) in both frequency bands which suggests both a large difference in seismic velocities and a short distance over which the change takes place. The C5 anomaly shows some multipathing (40%, M6 in Figure 8a) near the

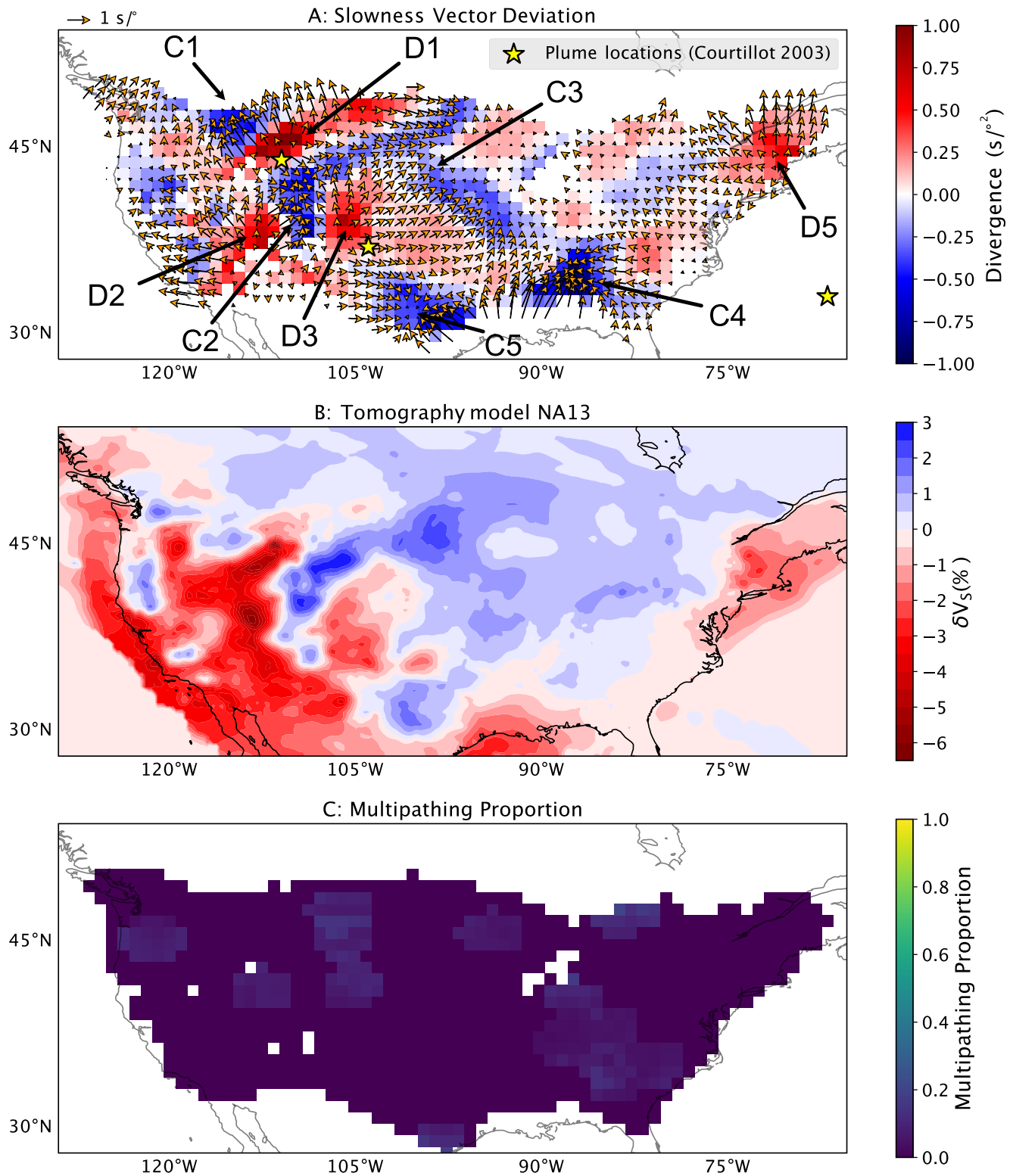


**Figure 7.** Figure of (a) slowness vector deviation bins at 200 km depth with the divergence in the background Plume locations from Courtillet et al. (2003) are shown as yellow stars. The background is the divergence of the slowness deviation vector field calculated using Equation 3. (b) velocity structure of tomography model NA13 (Bede et al., 2021) at 200 km depth, and (c) multipathing proportions in the 0.10–0.20 Hz frequency band using pierce points at 200 km depth beneath the US. The bins have a radius of 200 km with a spacing of 100 km.

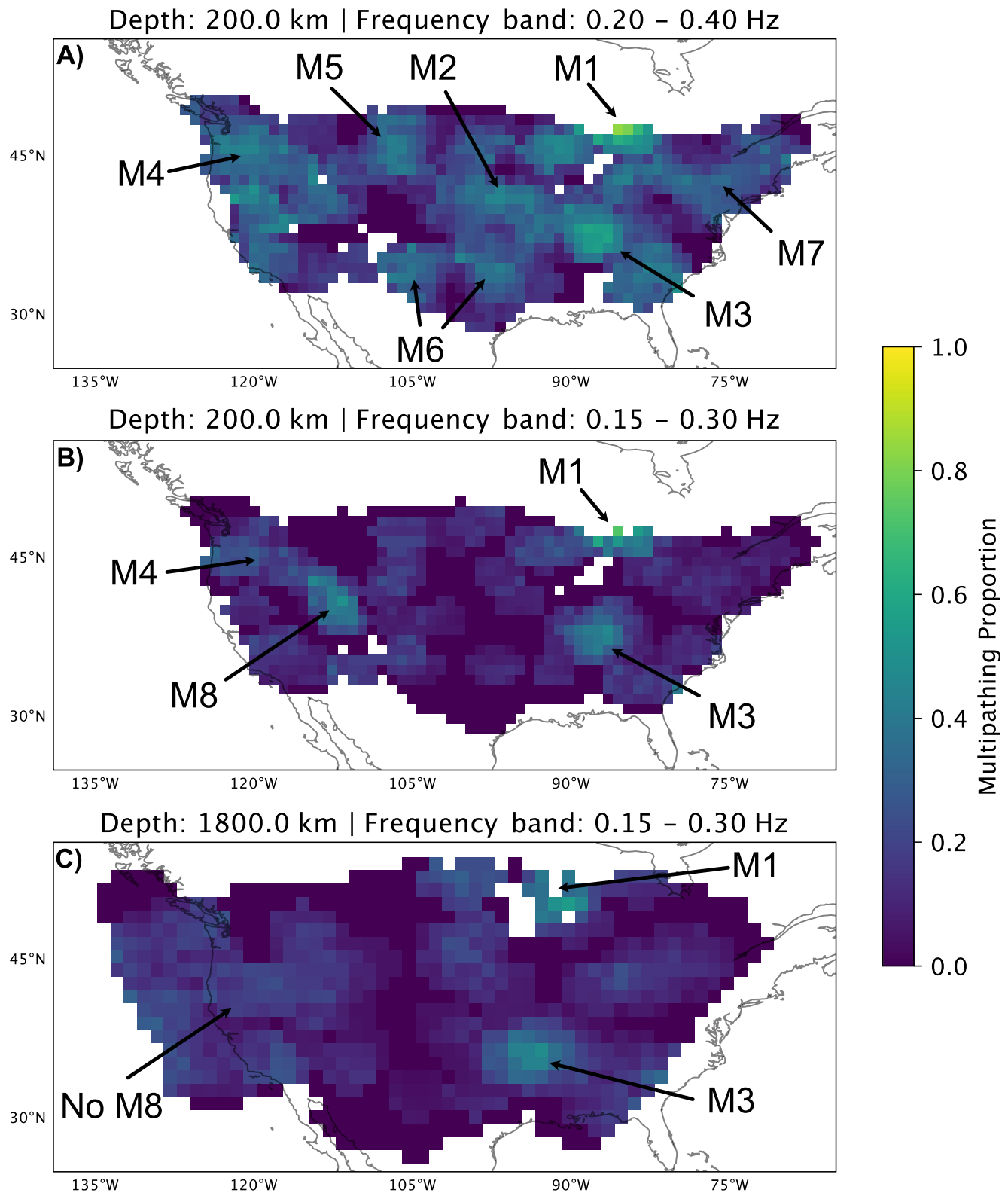


**Figure 8.** Proportion of multipathing observations relative to the total number of observations per bin. The sub-figures show different depth slices and frequency bands. (a) 200 km depth and band 0.20–0.40 Hz, (b) 200 km and band 0.15–0.30 Hz, (c) 1,800 km depth and band 0.15–0.30 Hz. This highlights the difference in the distribution of multipathing in the upper mantle between frequency bands (a) and (b) and the disappearance of multipathing proportion M8 with depth (b) and (c). Bins for the multipathing proportion measurements are 200 km radius, spaced with increments of 100 km.



boundaries of the diverging regions in the highest frequency band only. We interpret this as the anomalies boundaries causing multipathing, but the velocity gradient exists on a scale of at most 470 km.

In the northeast of the US, we observe a region with diverging slowness vectors (D5) beneath the Appalachian mountains, indicative of seismically slow material. This region does show some multipathing at the boundaries of the diverging region (M7) suggesting a transition in terms of temperature or composition on the scale of at most 470 km. We discuss the possible origins of this structure later.

West of the D5 anomaly, we observe a sharp change in slowness vector magnitudes from approximately  $1 \text{ s}^\circ$  to very small deviations giving a negative divergence (C3; Figure 7a). The large slowness vector magnitudes of C3 indicate a lateral velocity gradient or heterogeneity but, as there is a distinct transition to negligible magnitudes, only one strong velocity gradient may be present. The region does show some multipathing in the highest frequency band (M2 in Figure 8a). We speculate this could be the boundary of the North American craton with the transition occurring over at most 470 km.

A high multipathing proportion is observed in many regions when the data is projected to 200 km depth but only observed in the higher frequency band (Figure 8a) with very little multipathing observed in the lowest frequency band (Figure 10c). This suggests the heterogeneity causing this multipathing is of a sufficiently small scale to only be imaged by the short-wavelength observations. Not all multipathing will be caused at this depth, but we argue a significant proportion will be, because of the high number of low variance bins in the upper mantle (Figure 5). We suggest this multipathing may be caused by structures that are not individually resolvable by seismic tomography or do not cause multipathing in lower frequency bands. We interpret these structures to have velocity gradients with scales of at most 470 km.

In the lower mantle (Figure 9), there are regions of diverging slowness vector (D7 and D8) which may be indicative of low-velocity structure. However, the effects of upper mantle structure affecting lower mantle observations mean interpreting the data for lower mantle structure is challenging. We discuss this further in Section 4.3. The wide distribution of high-frequency multipathing in the upper mantle is also observed throughout the lowermost mantle beneath North America (although at a slightly lower proportion; Figure 9), but we do not observe large slowness vector magnitudes or patterns in this region. We suggest most of the multipathing is caused by structure in the upper and mid mantle; it is challenging to discern the origin, however.

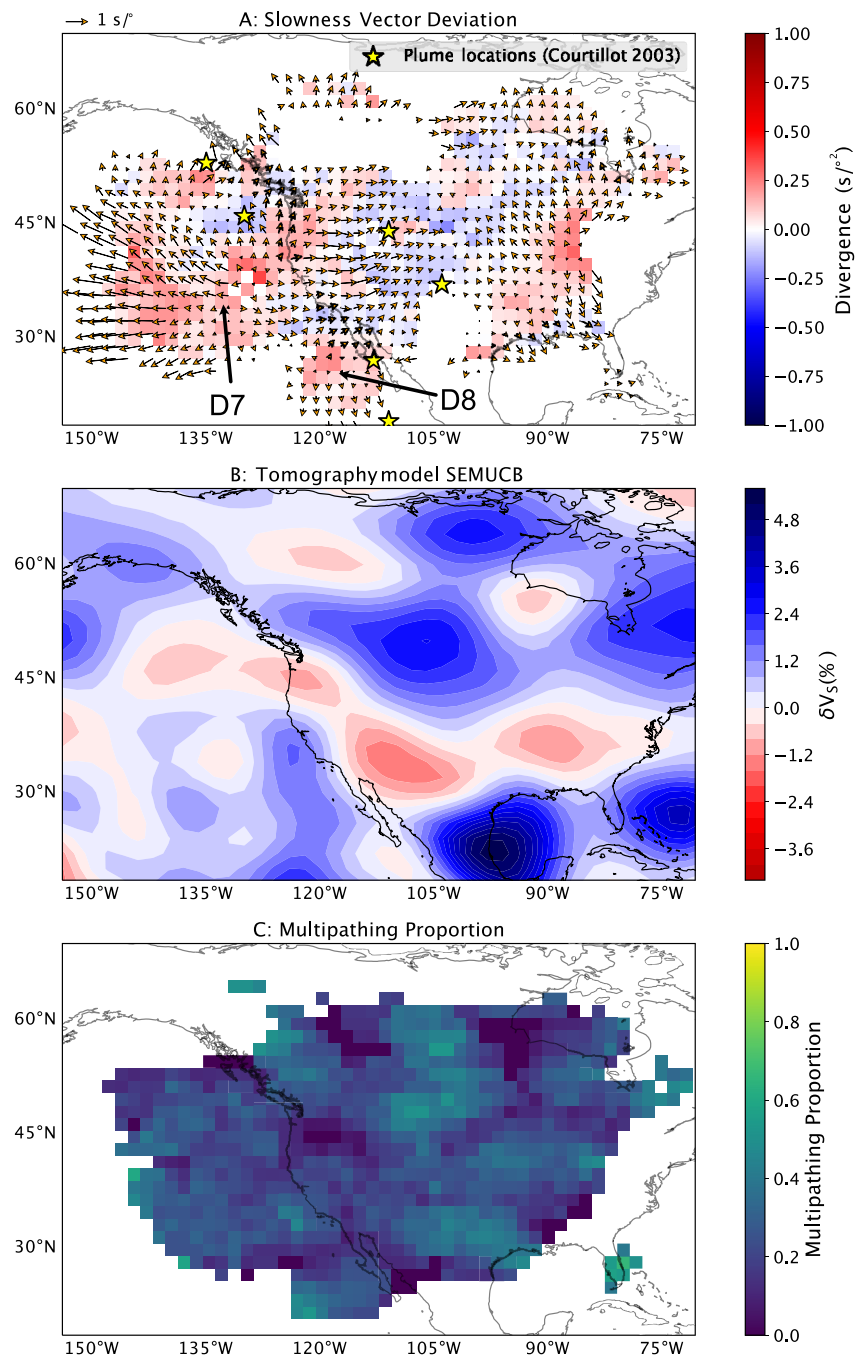
Many depths and frequency bands show a very high proportion (80%) of multipathing which we label M1 in Figure 8, but there is very little slowness vector deviation in either the binned or the unbinned data. We do not know what could be causing such a high multipathing proportion with small slowness vector magnitudes. Future work on a detailed regional analysis to investigate whether combinations of seismically fast and slow mantle structures could lead to these observations or if structures in the near surface could be the cause.

### 4.3. Comparison With Tomography Models

Many tomography models have been presented to understand the upper mantle beneath the US (e.g., Porritt et al., 2014; Schmandt & Lin, 2014; Sigloch et al., 2008; Tian et al., 2011). In this section, we compare our observations to those created by ray tracing through three velocity models of the upper mantle to determine how much upper mantle structure is contributing to our observations and test the tomography models against our observations. Our observations provide a good test for these models as SKS data are not used to make the models and slowness vector measurements are not incorporated into the inversion.

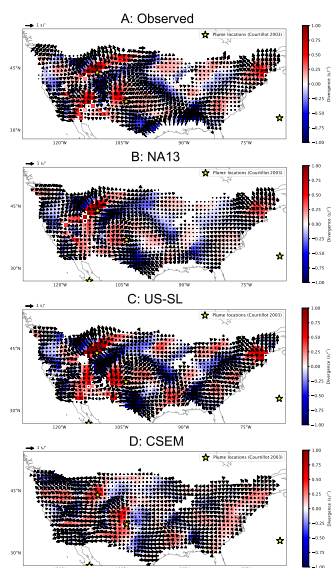
We choose the models from Fichtner et al. (2018), Schmandt and Lin (2014) and Bedle et al. (2021) because they use different approaches and data. These velocity models are for the upper to mid mantle only (depths of up to 500–1,200 km) and do not contain lower mantle structure. For the core and lower mantle, we use velocities from 1D earth model AK135 (Kennett et al., 1995) as this is the reference model used to convert Schmandt and Lin (2014) to absolute velocities and for consistency we use this structure for the other models. We use the same ray tracing software as described in Section 4.1 to calculate the travel times for each source-receiver pair in the data set. We then place a Ricker wavelet at the calculated travel time and use beamforming (Rost & Thomas, 2002) to find the slowness vector with the maximum power. From these slowness vector measurements, the same binning process as described earlier is applied.

Figure 10 presents the slowness vector bins at 200 km depth where the variance analysis suggests most of the signal is being caused by structures at this depth. Visual inspection of Figure 10 shows the results from all models



**Figure 9.** Figure of (a) slowness vector deviation bins at 2891 km depth with the divergence in the background. Plume locations from Courtillot et al. (2003) are shown as yellow stars. The background shows the divergence of the slowness deviation vector field calculated using Equation 3. (b) velocity structure of tomography model SEMUCB (French & Romanowicz, 2014) at 2,891 km depth, and (c) multipathing proportions in the 0.20–0.40 Hz frequency band using pierce points at 2,891 km depth beneath the US. The bins have a radius of 200 km with a spacing of 100 km.

are able to reproduce the general structure of the data but all show differences on a finer scale. The CSEM model (Fichtner et al., 2018) was made using full waveform inversion (FWI) and, in theory, could use the same information as this study to create their velocity model. We argue using slowness vector measurements as we have here is still useful due to the higher frequencies useable, the lower computational cost and are able to use noisier data. Our preferred model is NA13 (Bedle et al., 2021) as it recovers the same converging and diverging patterns better than the CSEM model (Fichtner et al., 2018) and has more realistic slowness vector deviation magnitudes than



**Figure 10.** A comparison of (a) observed slowness vector deviation bins with the divergence in the background at 200 km depth, (b) synthetic results of the ray tracing using tomography model NA13 (Bede et al., 2021) at 200 km depth, (c) tomography model US-SL (Schmandt & Lin, 2014), and (d) tomography model CSEM (Fichtner et al., 2018) at 200 km depth beneath the US. The bins have a radius of 200 km with a spacing of 100 km. Plume locations from Courtillot et al. (2003) are shown as yellow stars. Background for each of the plots shows the divergence of the slowness deviation vector field calculated using Equation 3.

US-SL (Schmandt & Lin, 2014). There are differences with the observations still where the model produces lower magnitude slowness vector deviations indicating structure is not resolved by the tomography model. The differences show there is information in our observations about mantle structure not included in the tomography and therefore the value of analyzing the mantle using slowness vector measurements.

As lower mantle structure is not present in the models we can infer the effect of upper mantle structure on our observations of lower mantle structure. We find that the signal for all three models in the lowermost mantle is similar to that in the observations (Figure 11). Therefore, we conclude the apparent signal in the lowermost is caused by heterogeneity in the upper mantle beneath the US.

## 5. Geological Interpretation

Our slowness vector deviation observations agree well with the velocity structure of tomography model NA13 (Bede et al., 2021) and as such our interpretation of the seismically slow and fast anomaly locations would be similar. Multipathing provides different information to the slowness vector measurement and tomography studies. Multipathing is indicative of sharp lateral velocity gradients and the frequency band in which multipathing is observed can give further information on the spatial scales at which the gradient exists. Therefore, we focus our interpretation on the meaning of our multipathing observations in the context of the origin and nature of possible mantle upwellings and the origin of the seismically fast material we observe.

### 5.1. Upwellings Beneath the US

In our interpretation, we assume the seismically slow regions identified are likely to be hot and therefore have a positive buoyancy and likely to be upwellings. From our divergence maps, we observe four regions of diverging slowness vector deviations which we interpret as upwellings beneath Yellowstone (D1), Appalachian mountains (D5), beneath the Colorado plateau (D3) and beneath southwest Utah (D2). These anomalies show unique multipathing behavior.

#### 5.1.1. Yellowstone

The Yellowstone anomaly is a heavily studied region of intra-plate volcanism with some controversy over its origin. Some suggest it is of shallow origin (Christiansen et al., 2002; Leonard & Liu, 2016) while others have suggested a deeply rooted plume (Nelson & Grand, 2018). Our observations are unable to determine if there is a lower mantle root as our lower mantle observations are strongly contaminated by signal in the upper mantle. The Yellowstone anomaly is often observed to have the seismically slowest anomaly in tomography models (e.g., Bede et al., 2021; Schmandt et al., 2012) and the temperatures inferred from these anomalies are greater than the melting point of peridotite at 50–100 km depth (Goes & Lee, 2002). Therefore, it is argued the Yellowstone anomaly is home to partial melt. Observations of attenuation suggest the upper 200 km beneath Yellowstone attenuates more strongly than deeper in the mantle and could be more hydrated (Adams & Humphreys, 2010).  $V_p/V_s$  ratios from tomography models agree the upper 200 km is distinct from deeper and may contain partial melt and be hydrated (Schmandt & Humphreys, 2010).

We observe multipathing at high frequencies at the boundaries of the Yellowstone anomaly (M4 and M5, Figure 8a), indicative of sharp velocity gradients at the boundaries and a distinct transition in composition or thermal properties. As previous studies have suggested the presence of partial melt in this region, we hypothesize the multipathing could be caused by a transition from a region with partial melt and high temperatures to a colder region without partial melt. Using the approach outlined in Section 2.4 we estimate the maximum transition length would be approximately 470 km.

#### 5.1.2. Small-Scale Upwellings

In addition to the Yellowstone anomaly, we interpret slowness vector deviations as evidence for smaller-scale low-velocity anomalies in the upper mantle as observed in previous studies (Eagar et al., 2010; Gilbert

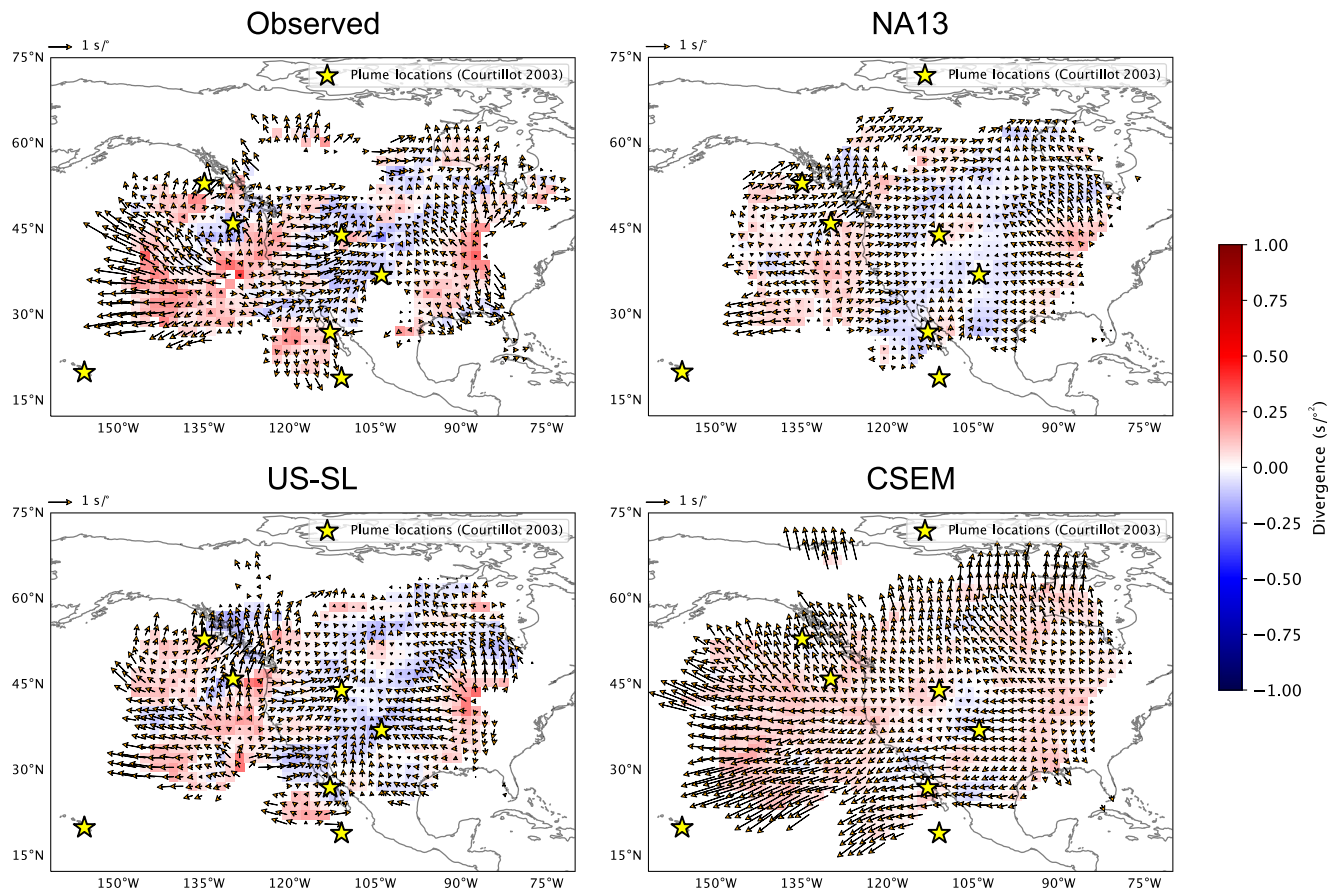


**Figure 11.** A comparison of the observed slowness vector deviation bins and divergence at 2,891 km depth (a) with the results of ray tracing from the tomography models discussed. These tomography models have no lower mantle structures and so are a good test of the effect of upper mantle structure when trying to infer potential lower mantle heterogeneities. The models are NA13 (Bedle et al., 2021) (b), tomography model US-SL (Schmandt & Lin, 2014) (c) and tomography model CSEM (Fichtner et al., 2018) (d) all projected to 2,891 km depth beneath the US. The bins have a radius of 200 km with a spacing of 100 km. plume locations from Courtillot et al. (2003) are shown as yellow stars. Background for each of the plots shows the divergence of the slowness deviation vector field calculated using Equation 3.

et al., 2003; Schmandt & Humphreys, 2010; Xue & Allen, 2007), labeled D2 and D3 in Figure 7. The D2 pattern is located east of where previous studies identify a “slab window” (Porritt et al., 2014; Sigloch et al., 2008; Tian et al., 2011) where the Farallon slab may have broken apart, possibly initiating small-scale upwelling from hydration melting and partial melt (Cao & Levander, 2010; Schmandt et al., 2012; Schmandt & Humphreys, 2010; Tian et al., 2009). We observe diverging region D3 which is possibly an upwelling to the east of the slab window. This region has a low multipathing proportion (Figure 8), counter to what we observe beneath Yellowstone. The difference could be due to differences in velocity gradients or depth extents of the structures.

### 5.1.3. North Appalachian Anomaly

The North Appalachian anomaly (NAA) has been imaged in several tomography models (e.g., Bedle et al., 2021; Schmandt & Lin, 2014; Yang & Gao, 2018; Zhou et al., 2022), spans over 400 km in diameter and is thought to have very low seismic velocities of approximately  $-10\%$  in  $V_s$  (Menke et al., 2016; Rychert et al., 2007). Some associate it with the Great Meteor hotspot (Taylor & Fitzgerald, 2011), but this may be the result of a coincidental geometry (Menke et al., 2016). The anomaly has been hypothesized to be related to lithosphere delamination (G. A. Houseman & Molnar, 1997; G. Houseman & Molnar, 2001). Our multipathing observations show a small proportion in the high-frequency band suggesting the anomaly transitions over a distance of at most 470 km. Any future hypotheses of the cause of this structure will need to be able to have sufficiently sharp boundaries to satisfy our observations.



## 5.2. Upper Mantle Fast Seismic Anomalies

The subduction history of the US is still a region of active debate and discussion, largely due to the complexity of mantle structure and how these structures interact. The upper mantle in the west can be broadly characterized as a large region of low velocity with high-velocity structures scattered throughout (Fichtner et al., 2018; Porritt et al., 2014; Schmandt & Lin, 2014). This, with observations of a thin low-velocity zone above the mantle transition zone at 410 km depth (Gao et al., 2006; Schmandt et al., 2011; Song et al., 2004; Vinnik et al., 2010), is interpreted as the Farallon slab subducting into the upper mantle, releasing water and causing partial melt and small-scale upwellings in the upper mantle (Cao & Levander, 2010; Schmandt et al., 2012; Schmandt & Humphreys, 2010; Tian et al., 2009). The Yellowstone plume is speculated to affect the Farallon slab by causing tears and gaps in the slab observed as patches of high-velocity regions (Leonard & Liu, 2016; Obrebski et al., 2010; Pierce & Morgan, 2009; Sigloch et al., 2008; Tian et al., 2011; Xue & Allen, 2007). Seismically fast material observed further to the east has been interpreted as lithospheric material with much discussion on its origin (Biryol et al., 2016; Liu et al., 2010; Wang et al., 2019). Like many tomography studies, we observe several seismically fast anomalies throughout the upper mantle. These fast anomalies show very different multipathing observations and in this section, we interpret these in the context of their subduction history.

### 5.2.1. Cascadia

Some tomography studies observe seismically fast material along the Cascadia subduction margin on the west coast of the US with a possible gap between the Juan de Fuca and Gorda slab (e.g., Bedle et al., 2021; Schmandt & Lin, 2014), which some suggest may be due to slab break off (Obrebski et al., 2011). The presence of this window is debated with some arguing it is an imaging artifact due to resolution limitations of the tomographic approaches (Roth et al., 2008) or affected by the starting velocity model (Long, 2016). Other studies have presented observations supportive of a continuous slab without a window with reflectors (Tauzin et al., 2016) and episodic tremor and slip (Audet et al., 2010). Our observations show multipathing is present all along the west coast of the US (M4, Figure 8a) at high frequencies which is compatible with both the broken and intact slab hypotheses.

### 5.2.2. Mid-Mantle Slabs

We observe evidence for seismically fast anomalies beneath the eastern US (C3 and C4) and where we observe multipathing regions M2 and M3. There is much speculation on the origin of the C4 anomaly, where we observe evidence for a fast anomaly agreeing with several tomography models (Porritt et al., 2014; Schmandt et al., 2011; Schmandt & Lin, 2014; Sigloch et al., 2008). Some suggest it could be a Farallon slab fragment of age 40 Ma which has stagnated above the 660 km transition (Liu & Stegman, 2011; Sigloch et al., 2008). Other suggest it could be a Grenville slab fragment again stagnating in the mid-mantle. Some find by inverse convection models and plate reconstruction models that these align palaeogeographically with the Shatsky and Hess conjugate plateau as they subducted beneath North America (Liu et al., 2010). All of these require a mechanism for slab stagnation where other slabs have descended deeper. As neither are attached to the crust some mechanism for neutral buoyancy or a barrier at 660 km is needed. Alternatively, there is a suggestion of dense lithosphere delamination or a dripping process where lithosphere drops into the mantle by a Raleigh-Taylor instability (Biryol et al., 2016; G. A. Houseman & Molnar, 1997).

Like the C4 anomaly in the east, we observe a distinct region of multipathing in the central frequency band (0.15–0.30 Hz) near anomalies C2 southeast of Yellowstone (Figure 7a). We interpret this as the boundaries of the C4 and C2 heterogeneities having a large velocity contrast and also transitioning over a longer distance. These anomalies have been imaged as fast anomalies between the 410 and 660 km deep transition zone in several tomography models (Bedle et al., 2021; Porritt et al., 2014; Schmandt & Lin, 2014; Sigloch et al., 2008; Wang et al., 2019). We interpret this as possible lithosphere which has descended into the mid mantle and is sufficiently old that it has been heated by the mantle and has weaker thermal gradients at its boundaries. These weaker gradients are able to produce multipathing in the central frequency band and we estimate the transition length of the boundaries is at most 510 km.

## 6. Future Work

The results presented in this study show continent-scale observations of slowness vector deviations and multipathing can be made automatically, can resolve seismically slow and fast anomalies and identify sharp boundaries



not easily resolved by tomography models. Better imaging can be achieved by extending the analysis to include direct arrivals, core reflected waves, core diffracted and other core refracted phases. This would then further constrain the location of mantle heterogeneity and sharp velocity gradients. As discussed above, some heterogeneities previously observed as fast anomalies within the transition zone (410–660 km depth) show high proportions of multipathing in the central frequency band (Figure 8). We speculate this may be due to weaker velocity gradients around the slab as it passes through the mantle and warms. Using multipathing signatures of fast seismic anomalies may be able to give more information on their thermal state and contribute to the question of why some stagnate while others do not. As each heterogeneity seemingly has a unique combination of multipathing and slowness vector observations, forward modeling could effectively constrain the morphology, velocity gradient properties and velocity perturbation of these anomalies with care taken to account for dipping boundaries (Niazi, 1966).

Slowness vector measurements can be made automatically on a continental scale and larger. These measurements are not currently included in a tomographic inversion, but we now argue these provide complementary information to travel times and could improve the resolution in the inversion. In the forward modeling, the velocity vector could be measured at the points where the slowness vector measurements are made by taking the spatial derivative of the travel times. This would then provide a suitable comparison that can be iteratively reduced in an inversion setup. As the slowness vector measurements were made using beamforming described earlier, they are sensitive to frequency and waveform information that travel time tomography is not. Furthermore, array-based methods can be used to identify paths where multipathing occurs which travel time tomography is not sensitive to. By adding slowness vector observations as a constraint, we argue tomographic inversions will be able to better resolve mantle heterogeneity.

## 7. Conclusions

We have presented the first continent-scale data set quantifying the deflection of teleseismic shear waves and multipathing caused by mantle heterogeneity. This study shows this scale of data set and larger can be created automatically. Our observations provide insight into the lateral velocity gradients throughout the mantle beneath the US, giving information on thermal or chemical gradients in the mantle. We confirm a frequency dependence of observable multipathing, observe a frequency dependence of slowness vector deviation magnitudes and show the divergence or convergence of the slowness vector deviation field can image fast and slow heterogeneity well. Multipathing in different frequency bands can be used to identify structures in the mantle. High-frequency multipathing observed widely across the upper mantle suggests velocity gradients are present with length scales of up to 470 km, but constraining the depths of SKS multipathing is challenging. Multipathing in the central frequency band is observed in local regions where fast anomalies have been observed in the mantle transition zone (e.g., Sigloch et al., 2008). We interpret these anomalies as being older than the other fast anomalies and have been warmed by the mantle, leading to weaker velocity gradients at their boundaries. By comparing our results to those created using ray-tracing through tomography models, we find our results are best replicated by model NA13 (Bedle et al., 2021) showing that slowness vector measurements are effective in resolving mantle structure. The differences between the observed and synthetic data show slowness vector measurements provide more constraints on mantle structure which could be incorporated into tomographic inversions.

## Data Availability Statement

The processed seismograms used to make the array measurements are stored as SAC (Goldstein et al., 2003) files are freely available on figshare via <https://doi.org/10.6084/m9.figshare.21701621> under a CC BY 4.0 license with a list of events used here <https://doi.org/10.6084/m9.figshare.21710564> and the results here <https://doi.org/10.6084/m9.figshare.21710603>. The data is taken as a subset from Thorne et al. (2020) which was collected using the SOD software (Owens et al., 2004) and the raw seismograms are freely available from the IRIS Data Management Centre with the dois for each network used provided in Supporting Information S1. Figures were made using Matplotlib (Hunter, 2007) and cartopy (Met Office, 2010–2015). Travel time and slowness predictions from 1D velocity models were made using the TauP toolkit (Crotwell et al., 1999). Code to make automated slowness vector measurements is publicly available from [https://github.com/eejwa/Array\\_Seis\\_Circle](https://github.com/eejwa/Array_Seis_Circle) (Ward, 2021).

## Acknowledgments

We thank the reviewers for taking the time to read and suggest corrections that improved the manuscript. JW is supported by the NERC DTP SPHERES Grant NE/L002574/1, AN was funded by NERC standard Grant NE/R001154/1 (REMIS: Reliable Earthquake Magnitudes for Induced Seismicity), AN and JW are supported by NERC large grant Mantle Circulation Constrained NE/T012684/1, SR was supported by NE/R012199/1 and MT was partially supported by NSF Grant EAR-1723081.

## References

- Abt, D. L., Fischer, K. M., French, S. W., Ford, H. A., Yuan, H., & Romanowicz, B. (2010). North American lithospheric discontinuity structure imaged by Ps and Sp receiver functions. *Journal of Geophysical Research*, 115(B9), B09301. <https://doi.org/10.1029/2009jb006914>
- Adams, D. C., & Humphreys, E. D. (2010). New constraints on the properties of the Yellowstone mantle plume from P and S wave attenuation tomography. *Journal of Geophysical Research*, 115(B12), B12311. <https://doi.org/10.1029/2009jb006864>
- Audet, P., Bostock, M. G., Boyarko, D. C., Brudzinski, M. R., & Allen, R. M. (2010). Slab morphology in the Cascadia fore arc and its relation to episodic tremor and slip. *Journal of Geophysical Research*, 115(B4), B00A16. <https://doi.org/10.1029/2008jb006053>
- Bedle, H., Lou, X., & Van der Lee, S. (2021). Continental tectonics inferred from high-resolution imaging of the mantle beneath the United States, through the combination of USArray data types. *Geochemistry, Geophysics, Geosystems*, 22(10), e2021GC009674. <https://doi.org/10.1029/2021GC009674>
- Benthams, H. L. M., Rost, S., & Thorne, M. S. (2017). Fine-scale structure of the mid-mantle characterised by global stacks of PP precursors. *Earth and Planetary Science Letters*, 472, 164–173. <https://doi.org/10.1016/j.epsl.2017.05.027>
- Biryol, C. B., Wagner, L. S., Fischer, K. M., & Hawman, R. B. (2016). Relationship between observed upper mantle structures and recent tectonic activity across the southeastern United States. *Journal of Geophysical Research: Solid Earth*, 121(5), 3393–3414. <https://doi.org/10.1002/2015jb012698>
- Bunge, H.-P., & Grand, S. P. (2000). Mesozoic plate-motion history below the northeast Pacific Ocean from seismic images of the subducted Farallon slab. *Nature*, 405(6784), 337–340. <https://doi.org/10.1038/35012586>
- Cao, A., & Levander, A. (2010). High-resolution transition zone structures of the Gorda Slab beneath the Western United States: Implication for deep water subduction. *Journal of Geophysical Research*, 115(B7), B07301. <https://doi.org/10.1029/2009jb006876>
- Capon, J. (1974). Characterization of crust and upper mantle structure under LASA as a random medium. *Bulletin of the Seismological Society of America*, 64(1), 235–266.
- Christiansen, R. L., Foulger, G., & Evans, J. R. (2002). Upper-mantle origin of the Yellowstone hotspot. *Geological Society of America Bulletin*, 114(10), 1245–1256. [https://doi.org/10.1130/0016-7606\(2002\)114<1245:umooty>2.0.co;2](https://doi.org/10.1130/0016-7606(2002)114<1245:umooty>2.0.co;2)
- Courtillot, V., Davaille, A., Besse, J., & Stock, J. (2003). Three distinct types of hotspots in the Earth's mantle. *Earth and Planetary Science Letters*, 205(3), 295–308. [https://doi.org/10.1016/s0012-821x\(02\)01048-8](https://doi.org/10.1016/s0012-821x(02)01048-8)
- Crotwell, H. P., Owens, T. J., & Ritsema, J. (1999). The TauP Toolkit: Flexible seismic travel-time and ray-path utilities. *Seismological Research Letters*, 70(2), 154–160. <https://doi.org/10.1785/gssrl.70.2.154>
- Deuss, A. (2009). Global observations of mantle discontinuities using SS and PP precursors. *Surveys in Geophysics*, 30(4–5), 301–326. <https://doi.org/10.1007/s10712-009-9078-y>
- Deuss, A., Redfern, S. A. T., Chambers, K., & Woodhouse, J. H. (2006). The nature of the 660-kilometer discontinuity in Earth's mantle from global seismic observations of PP precursors. *Science*, 311(5758), 198–201. <https://doi.org/10.1126/science.1120020>
- Dziewonski, A. M., & Anderson, D. L. (1981). Preliminary reference Earth model. *Physics of the Earth and Planetary Interiors*, 25(4), 297–356. [https://doi.org/10.1016/0031-9201\(81\)90046-7](https://doi.org/10.1016/0031-9201(81)90046-7)
- Eagar, K. C., Fouch, M. J., & James, D. E. (2010). Receiver function imaging of upper mantle complexity beneath the Pacific Northwest, United States. *Earth and Planetary Science Letters*, 297(1), 141–153. <https://doi.org/10.1016/j.epsl.2010.06.015>
- Efron, B. (1992). Bootstrap methods: Another look at the jackknife. In S. Kotz & N. L. Johnson (Eds.), *Breakthroughs in statistics: Methodology and distribution* (pp. 569–593). Springer.
- Ester, M., Krieger, H.-P., Sander, J., & Xu, X. (1996). A density-based algorithm for discovering clusters in large spatial databases with noise. In *Kdd-96 proceedings*, (Vol. 96, pp. 226–231).
- Fichtner, A., van Herwaarden, D.-P., Afanasiev, M., Simuté, S., Krischer, L., Çubuk Sabuncu, Y., et al. (2018). The collaborative seismic Earth model: Generation 1. *Geophysical Research Letters*, 45(9), 4007–4016. <https://doi.org/10.1029/2018gl077338>
- French, S., & Romanowicz, B. (2014). Whole-mantle radially anisotropic shear velocity structure from spectral-element waveform tomography. *Geophysical Journal International*, 199(3), 1303–1327. <https://doi.org/10.1093/gji/ggu334>
- Gao, W., Matzel, E., & Grand, S. P. (2006). Upper mantle seismic structure beneath eastern Mexico determined from P and S waveform inversion and its implications. *Journal of Geophysical Research*, 111(B8), B08307. <https://doi.org/10.1029/2006jb004304>
- Gilbert, H. J., Sheehan, A. F., Dueker, K. G., & Molnar, P. (2003). Receiver functions in the Western United States, with implications for upper mantle structure and dynamics. *Journal of Geophysical Research*, 108(B5). <https://doi.org/10.1029/2001jb001194>
- Goes, S., & Lee, S. V. d. (2002). Thermal structure of the North American uppermost mantle inferred from seismic tomography. *Journal of Geophysical Research*, 107(B3), ETG2–1–ETG2–13. <https://doi.org/10.1029/2000jb000049>
- Goldstein, P., Dodge, D., Firpo, M., Minner, L., Lee, W., Kanamori, H., et al. (2003). SAC2000: Signal processing and analysis tools for seismologists and engineers. *The IASPEI International Handbook of Earthquake and Engineering Seismology*, 81, 1613–1620.
- Grand, S. P., van der Hilst, R. D., & Widiyantoro, S. (1997). High resolution global tomography: A snapshot of convection in the Earth. *Geological Society of America Today*, 7(4).
- Hedlin, M. A. H., & Shearer, P. M. (2000). An analysis of large-scale variations in small-scale mantle heterogeneity using Global Seismographic Network recordings of precursors to PKP. *Journal of Geophysical Research*, 105(B6), 13655–13673. <https://doi.org/10.1029/2000jb900019>
- Houseman, G., & Molnar, P. (2001). Mechanisms of lithospheric rejuvenation associated with continental orogeny. *Geological Society, London, Special Publications*, 184(1), 13–38. <https://doi.org/10.1144/gsl.sp.2001.184.01.02>
- Houseman, G. A., & Molnar, P. (1997). Gravitational (Rayleigh–Taylor) instability of a layer with non-linear viscosity and convective thinning of continental lithosphere. *Geophysical Journal International*, 128(1), 125–150. <https://doi.org/10.1111/j.1365-246x.1997.tb04075.x>
- Hunter, J. D. (2007). Matplotlib: A 2D graphics environment. *Computing in Science & Engineering*, 9(3), 90–95. <https://doi.org/10.1109/MCSE.2007.55>
- Jenkins, J., Deuss, A., & Cottaar, S. (2017). Converted phases from sharp 1000 km depth mid-mantle heterogeneity beneath Western Europe. *Earth and Planetary Science Letters*, 459, 196–207. <https://doi.org/10.1016/j.epsl.2016.11.031>
- Kennett, B., Engdahl, E., & Buland, R. (1995). Constraints on seismic velocities in the Earth from traveltimes. *Geophysical Journal International*, 122(1), 108–124. <https://doi.org/10.1111/j.1365-246x.1995.tb03540.x>
- Kind, R., Yuan, X., Mechie, J., & Sodoudi, F. (2015). Structure of the upper mantle in the north-western and central United States from USArray S-receiver functions. *Solid Earth*, 6(3), 957–970. <https://doi.org/10.5194/se-6-957-2015>
- Krischer, L., Fichtner, A., Boehm, C., & Igel, H. (2018). Automated large-scale full seismic waveform inversion for North America and the North Atlantic. *Journal of Geophysical Research: Solid Earth*, 123(7), 5902–5928. <https://doi.org/10.1029/2017jb015289>
- Leonard, T., & Liu, L. (2016). The role of a mantle plume in the formation of Yellowstone volcanism. *Geophysical Research Letters*, 43(3), 1132–1139. <https://doi.org/10.1002/2015gl067131>

- Liu, L., Gurnis, M., Seton, M., Saleeby, J., Müller, R. D., & Jackson, J. M. (2010). The role of oceanic plateau subduction in the Laramide orogeny. *Nature Geoscience*, 3(5), 353–357. <https://doi.org/10.1038/ngeo829>
- Liu, L., & Stegman, D. R. (2011). Segmentation of the Farallon slab. *Earth and Planetary Science Letters*, 311(1–2), 1–10. <https://doi.org/10.1016/j.epsl.2011.09.027>
- Long, M. D. (2016). The Cascadia Paradox: Mantle flow and slab fragmentation in the Cascadia subduction system. *Journal of Geodynamics*, 102, 151–170. <https://doi.org/10.1016/j.jog.2016.09.006>
- Ma, X., & Thomas, C. (2020). Small-scale scattering heterogeneities in the lowermost mantle from a global analysis of PKP precursors. *Journal of Geophysical Research: Solid Earth*, 125(3), e2019JB018736. <https://doi.org/10.1029/2019jb018736>
- Maupin, V. (2011). Upper-mantle structure in southern Norway from beamforming of Rayleigh wave data presenting multipathing. *Geophysical Journal International*, 185(2), 985–1002. <https://doi.org/10.1111/j.1365-246x.2011.04989.x>
- Menke, W., Skryzalin, P., Levin, V., Harper, T., Darbyshire, F., & Dong, T. (2016). The northern Appalachian anomaly: A modern asthenospheric upwelling. *Geophysical Research Letters*, 43(19), 10173–10179. <https://doi.org/10.1002/2016gl070918>
- Met Office. (2010–2015). Cartopy: A cartographic python library with a Matplotlib interface. [Computer software manual]. Retrieved from <https://scitools.org.uk/cartopy>
- Nelson, P. L., & Grand, S. P. (2018). Lower-mantle plume beneath the Yellowstone hotspot revealed by core waves. *Nature Geoscience*, 11(4), 280–284. <https://doi.org/10.1038/s41561-018-0075-y>
- Ni, S., & Helmberger, D. V. (2003). Ridge-like lower mantle structure beneath South Africa. *Journal of Geophysical Research*, 108(B2). <https://doi.org/10.1029/2001jb001545>
- Ni, S., Tan, E., Gurnis, M., & Helmberger, D. (2002). Sharp sides to the African superplume. *Science*, 296(5574), 1850–1852. <https://doi.org/10.1126/science.1070698>
- Niazi, M. (1966). Corrections to apparent azimuths and travel-time gradients for a dipping Mohorovičić discontinuity. *Bulletin of the Seismological Society of America*, 56(2), 491–509. <https://doi.org/10.1785/bssa0560020491>
- Obrebski, M., Allen, R. M., Pollitz, F., & Hung, S.-H. (2011). Lithosphere–asthenosphere interaction beneath the Western United States from the joint inversion of body-wave traveltimes and surface-wave phase velocities. *Geophysical Journal International*, 185(2), 1003–1021. <https://doi.org/10.1111/j.1365-246x.2011.04990.x>
- Obrebski, M., Allen, R. M., Xue, M., & Hung, S.-H. (2010). Slab-plume interaction beneath the Pacific Northwest. *Geophysical Research Letters*, 37(14). <https://doi.org/10.1029/2010gl043489>
- Owens, T. J., Crotwell, H. P., Groves, C., & Oliver-Paul, P. (2004). SOD: Standing order for data. *Seismological Research Letters*, 75(4), 515–520. <https://doi.org/10.1785/gssrl.75.4.515-a>
- Pierce, K. L., & Morgan, L. A. (2009). Is the track of the Yellowstone hotspot driven by a deep mantle plume?—Review of volcanism, faulting, and uplift in light of new data. *Journal of Volcanology and Geothermal Research*, 188(1), 1–25. <https://doi.org/10.1016/j.jvolgeores.2009.07.009>
- Porritt, R. W., Allen, R. M., & Pollitz, F. F. (2014). Seismic imaging east of the Rocky Mountains with USArray. *Earth and Planetary Science Letters*, 402, 16–25. <https://doi.org/10.1016/j.epsl.2013.10.034>
- Ricker, N. (1943). Further developments in the wavelet theory of seismogram structure. *Bulletin of the Seismological Society of America*, 33(3), 197–228. <https://doi.org/10.1785/bssa0330030197>
- Ricker, N. (1944). Wavelet functions and their polynomials. *Geophysics*, 9(3), 314–323. <https://doi.org/10.1190/1.1445082>
- Ritsema, J., Kaneshima, S., & Haugland, S. M. (2020). The dimensions of scatterers in the lower mantle using USArray recordings of S-wave to P-wave conversions. *Physics of the Earth and Planetary Interiors*, 306, 106541. <https://doi.org/10.1016/j.pepi.2020.106541>
- Rodgers, A., Krischer, L., Afanasiev, M., Boehm, C., Doody, C., Chiang, A., & Simmons, N. (2022). WUS256: An adjoint waveform tomography model of the crust and upper mantle of the Western United States for improved waveform simulations. *Journal of Geophysical Research: Solid Earth*, 127(7), e2022JB024549. <https://doi.org/10.1029/2022jb024549>
- Rost, S., & Thomas, C. (2002). Array seismology: Methods and applications. *Reviews of Geophysics*, 40(3), 2–1–2–27. <https://doi.org/10.1029/2000rg000100>
- Roth, J. B., Fouch, M. J., James, D. E., & Carlson, R. W. (2008). Three-dimensional seismic velocity structure of the northwestern United States. *Geophysical Research Letters*, 35(15), L15304. <https://doi.org/10.1029/2008gl034669>
- Rychert, C. A., Rondenay, S., & Fischer, K. M. (2007). P-to-S and S-to-P imaging of a sharp lithosphere–asthenosphere boundary beneath eastern North America. *Journal of Geophysical Research*, 112(B8), B08314. <https://doi.org/10.1029/2006jb004619>
- Schmandt, B., Dueker, K., Humphreys, E., & Hansen, S. (2012). Hot mantle upwelling across the 660 beneath Yellowstone. *Earth and Planetary Science Letters*, 331–332, 224–236. <https://doi.org/10.1016/j.epsl.2012.03.025>
- Schmandt, B., Dueker, K. G., Hansen, S. M., Jasinsek, J. J., & Zhang, Z. (2011). A sporadic low-velocity layer atop the Western U.S. mantle transition zone and short-wavelength variations in transition zone discontinuities. *Geochemistry, Geophysics, Geosystems*, 12(8). <https://doi.org/10.1029/2011gc003668>
- Schmandt, B., & Humphreys, E. (2010). Complex subduction and small-scale convection revealed by body-wave tomography of the Western United States upper mantle. *Earth and Planetary Science Letters*, 297(3), 435–445. <https://doi.org/10.1016/j.epsl.2010.06.047>
- Schmandt, B., Jacobsen, S. D., Becker, T. W., Liu, Z., & Dueker, K. G. (2014). Dehydration melting at the top of the lower mantle. *Science*, 344(6189), 1265–1268. <https://doi.org/10.1126/science.1253358>
- Schmandt, B., & Lin, F.-C. (2014). P and S wave tomography of the mantle beneath the United States. *Geophysical Research Letters*, 41(18), 6342–6349. <https://doi.org/10.1002/2014gl016231>
- Shen, W., & Ritzwoller, M. H. (2016). Crustal and uppermost mantle structure beneath the United States. *Journal of Geophysical Research: Solid Earth*, 121(6), 4306–4342. <https://doi.org/10.1002/2016jb012887>
- Sigloch, K., McQuarrie, N., & Nolet, G. (2008). Two-stage subduction history under North America inferred from multiple-frequency tomography. *Nature Geoscience*, 1(7), 458–462. <https://doi.org/10.1038/ngeo231>
- Simmons, N., Myers, S., & Johannesson, G. (2011). Global-scale P wave tomography optimized for prediction of teleseismic and regional travel times for Middle East events: 2. Tomographic inversion. *Journal of Geophysical Research*, 116(B4), B04305. <https://doi.org/10.1029/2010jb007969>
- Simmons, N., Myers, S. C., Johannesson, G., & Matzel, E. (2012). LLNL-G3Dv3: Global P wave tomography model for improved regional and teleseismic travel time prediction. *Journal of Geophysical Research*, 117(B10). <https://doi.org/10.1029/2012jb009525>
- Song, A. T.-R., Helmberger, D. V., & Grand, S. P. (2004). Low-velocity zone atop the 410-km seismic discontinuity in the northwestern United States. *Nature*, 427(6974), 530–533. <https://doi.org/10.1038/nature02231>
- Sun, D., Helmberger, D., Lai, V. H., Gurnis, M., Jackson, J. M., & Yang, H.-Y. (2019). Slab control on the northeastern edge of the mid-Pacific LLSVP near Hawaii. *Geophysical Research Letters*, 46(6), 3142–3152. <https://doi.org/10.1029/2018gl081130>

- Sun, D., Helmberger, D., Ni, S., & Bower, D. (2009). Direct measures of lateral velocity variation in the deep Earth. *Journal of Geophysical Research*, 114(B5), B05303. <https://doi.org/10.1029/2008jb005873>
- Tao, Z., Li, A., & Fischer, K. M. (2020). Hotspot signatures at the North American passive margin. *Geology*, 49(5), 525–530. <https://doi.org/10.1130/g47994.1>
- Tauzin, B., Bodin, T., Debayle, E., Perrillat, J.-P., & Reynard, B. (2016). Multi-mode conversion imaging of the subducted Gorda and Juan de Fuca plates below the North American continent. *Earth and Planetary Science Letters*, 440, 135–146. <https://doi.org/10.1016/j.epsl.2016.01.036>
- Taylor, J. P., & Fitzgerald, P. G. (2011). Low-temperature thermal history and landscape development of the eastern Adirondack Mountains, New York: Constraints from apatite fission-track thermochronology and apatite (U-Th)/He dating. *Bulletin*, 123(3–4), 412–426. <https://doi.org/10.1130/b30138.1>
- Thorne, M. S., Leng, K., Pachhai, S., Rost, S., Wicks, J., & Nissen-Meyer, T. (2021). The most parsimonious ultralow-velocity zone distribution from highly anomalous SPdKS waveforms. *Geochemistry, Geophysics, Geosystems*, 22(1), e2020GC009467. <https://doi.org/10.1029/2020gc009467>
- Thorne, M. S., Pachhai, S., Leng, K., Wicks, J. K., & Nissen-Meyer, T. (2020). New candidate ultralow-velocity zone locations from highly anomalous SPdKS waveforms. *Minerals*, 10(3), 211. <https://doi.org/10.3390/min10030211>
- Tian, Y., Sigloch, K., & Nolet, G. (2009). Multiple-frequency SH-wave tomography of the Western US upper mantle. *Geophysical Journal International*, 178(3), 1384–1402. <https://doi.org/10.1111/j.1365-246x.2009.04225.x>
- Tian, Y., Zhou, Y., Sigloch, K., Nolet, G., & Laske, G. (2011). Structure of North American mantle constrained by simultaneous inversion of multiple-frequency SH, SS, and Love waves. *Journal of Geophysical Research*, 116(B2), B02307. <https://doi.org/10.1029/2010jb007704>
- Valentine, A. P., & Woodhouse, J. H. (2010). Approaches to automated data selection for global seismic tomography. *Geophysical Journal International*, 182(2), 1001–1012. <https://doi.org/10.1111/j.1365-246x.2010.04658.x>
- Vinnik, L. P., Oreshin, S. I., Speziale, S., & Weber, M. (2010). Mid-mantle layering from SKS receiver functions. *Geophysical Research Letters*, 37(24). <https://doi.org/10.1029/2010gl045323>
- Wang, H., Zhao, D., Huang, Z., & Wang, L. (2019). Tomography, seismotectonics, and mantle dynamics of central and eastern United States. *Journal of Geophysical Research: Solid Earth*, 124(8), 8890–8907. <https://doi.org/10.1029/2019jb017478>
- Ward, J. (2021). Array\_Seis\_Circle: Alpha release. <https://doi.org/10.5281/zenodo.7973945>
- Ward, J., Nowacki, A., & Rost, S. (2020). Lateral velocity gradients in the African lower mantle inferred from slowness space observations of multipathing. *Geochemistry, Geophysics, Geosystems*, 21(8), e2020GC009025. <https://doi.org/10.1029/2020gc009025>
- Ward, J., Thorne, M., Nowacki, A., & Rost, S. (2021). Automatic slowness vector measurements of seismic arrivals with uncertainty estimates using bootstrap sampling, array methods and unsupervised learning. *Geophysical Journal International*, 226(3), 1847–1857. <https://doi.org/10.1093/gji/ggab196>
- Waszek, L., Schmerr, N. C., & Ballmer, M. D. (2018). Global observations of reflectors in the mid-mantle with implications for mantle structure and dynamics. *Nature Communications*, 9(1), 385. <https://doi.org/10.1038/s41467-017-02709-4>
- Waszek, L., Thomas, C., & Deuss, A. (2015). PKP precursors: Implications for global scatterers. *Geophysical Research Letters*, 42(10), 3829–3838. <https://doi.org/10.1002/2015gl063869>
- Xue, M., & Allen, R. M. (2007). The fate of the Juan de Fuca plate: Implications for a Yellowstone plume head. *Earth and Planetary Science Letters*, 264(1), 266–276. <https://doi.org/10.1016/j.epsl.2007.09.047>
- Yang, X., & Gao, H. (2018). Full-wave seismic tomography in the northeastern United States: New insights into the uplift mechanism of the Adirondack Mountains. *Geophysical Research Letters*, 45(12), 5992–6000. <https://doi.org/10.1029/2018gl078438>
- Yuan, H., French, S., Cupillard, P., & Romanowicz, B. (2014). Lithospheric expression of geological units in central and eastern North America from full waveform tomography. *Earth and Planetary Science Letters*, 402, 176–186. <https://doi.org/10.1016/j.epsl.2013.11.057>
- Zhao, C., Garnero, E. J., McNamara, A. K., Schmerr, N., & Carlson, R. W. (2015). Seismic evidence for a chemically distinct thermochemical reservoir in Earth's deep mantle beneath Hawaii. *Earth and Planetary Science Letters*, 426, 143–153. <https://doi.org/10.1016/j.epsl.2015.06.012>
- Zhao, D., Hasegawa, A., & Horiuchi, S. (1992). Tomographic imaging of P and S wave velocity structure beneath northeastern Japan. *Journal of Geophysical Research*, 97(B13), 19909–19928. <https://doi.org/10.1029/92jb00603>
- Zhou, T., Li, J., Xi, Z., Li, G., & Chen, M. (2022). CUSRA2021: A radially anisotropic model of the contiguous US and surrounding regions by full-waveform inversion. *Journal of Geophysical Research: Solid Earth*, 127(8), e2021JB023893. <https://doi.org/10.1029/2021jb023893>